

1 **Anomalous dynamics of the extremely compressed magnetosphere during 21**  
2 **January 2005 magnetic storm**

3

4 A.V. Dmitriev<sup>1,2</sup>, A. V. Suvorova<sup>1,2</sup>, J.-K. Chao<sup>1</sup>, C. B. Wang<sup>3</sup>, L. Rastaetter<sup>4</sup>, M. I. Panasyuk<sup>2</sup>, L. L.  
5 Lazutin<sup>2</sup>, A. S. Kovtyukh<sup>2</sup>, I. S. Veselovsky<sup>2,5</sup>, I. N. Myagkova<sup>2</sup>

6 <sup>1</sup>*Institute of Space Science, National Central University, Chung-Li, Taiwan*

7 <sup>2</sup>*Lomonosov Moscow State University Skobeltsyn Institute of Nuclear Physics (MSU SINP), Moscow,*  
8 *Russia*

9 <sup>3</sup>*CAS Key Lab of Geospace Environment, Department of Geophysics and Planetary Science,*  
10 *University of Science and Technology of China, Hefei, China*

11 <sup>4</sup>*Goddard Space Flight Center, Maryland, USA*

12 <sup>5</sup>*Space Research Institute (IKI), Russian Academy of Sciences, Moscow, Russia*

13

14

15

16

17 Short title: EXTREME MAGNETOSPHERIC COMPRESSION

18

19

20

21

22

23

24

25

26

27

28 \_\_\_\_\_

29 A. V. Dmitriev, Institute of Space Science, National Central University, Chung-Li, 320, Taiwan, also  
30 at Lomonosov Moscow State University Skobeltsyn Institute of Nuclear Physics (MSU SINP),  
31 Russia (e-mail: dalex@jupiter.ss.ncu.edu.tw)

32 A. V. Suvorova, Institute of Space Science, National Central University, Chung-Li, 320, Taiwan, also  
33 at Lomonosov Moscow State University Skobeltsyn Institute of Nuclear Physics (MSU SINP),  
34 Russia (e-mail: alla@jupiter.ss.ncu.edu.tw)

35 J.-K. Chao, Institute of Space Science, National Central University, Chung-Li, 320, Taiwan (e-mail:  
36 jkchao@jupiter.ss.ncu.edu.tw)

37 C. B. Wang, CAS Key Lab of Geospace Environment, Department of Geophysics and Planetary  
38 Science, University of Science and Technology of China, Hefei, China. (e-mail:  
39 cbwang@ustc.edu.cn)

40 L. Rastaetter, Goddard Space Flight Center, Maryland, USA (e-mail: Lutz.Rastaetter@nasa.gov)

41 M. I. Panasyuk, Lomonosov Moscow State University Skobeltsyn Institute of Nuclear Physics (MSU  
42 SINP), Russia (e-mail: panasyuk@srdmail.sinp.msu.ru)

43 L. L. Lazutin, Lomonosov Moscow State University Skobeltsyn Institute of Nuclear Physics (MSU  
44 SINP), Russia (e-mail: ll@rd.sinp.msu.ru)

45 A. S. Kovtyukh, Lomonosov Moscow State University Skobeltsyn Institute of Nuclear Physics (MSU  
46 SINP), Russia (e-mail: kovtyukhas@mail.ru)

47 I. S. Veselovsky, Lomonosov Moscow State University Skobeltsyn Institute of Nuclear Physics  
48 (MSU SINP), also at Space Research Institute (IKI), Russian Academy of Sciences, Moscow, Russia  
49 (e-mail: veselov@dec1.sinp.msu.ru)

50 I. N. Myagkova, Lomonosov Moscow State University Skobeltsyn Institute of Nuclear Physics (MSU  
51 SINP), Russia (e-mail: irina@srd.sinp.msu.ru)

52

53 **Abstract**

54 Dynamics of the dayside magnetosphere and proton radiation belt was analyzed during unusual  
55 magnetic storm on 21 January 2005. We have found that during the storm from 1712 to 2400 UT, the  
56 subsolar magnetopause was continuously located inside geosynchronous orbit due to strong  
57 compression. The compression was found to be extremely strong from 1846 to 2035 UT when the  
58 dense plasma of fast erupting filament produced the solar wind dynamic pressure  $Pd$  peaked up to  
59  $>100$  nPa and, in the first time, the upstream solar wind was observed at geosynchronous orbit during  
60 almost 2 hours. Under the extreme compression, the outer magnetosphere at  $L > 5$  was pushed inward  
61 and the outer radiation belt particles with energies of several tens of keV moved earthward, became  
62 adiabatically accelerated and accumulated in the inner magnetosphere at  $L < 4$  that produced the  
63 intensified ring current with an exceptionally long lifetime. The observations were compared with  
64 predictions of various empirical and first principles models. All the models failed to predict the  
65 magnetospheric dynamics under the extreme compression when the minimal magnetopause distance  
66 was estimated to be  $\sim 3$  Re. The inconsistencies between the model predictions and observations  
67 might result from distortions of plasma measurements by extreme heliospheric conditions consisting  
68 in very fast solar wind streams ( $\sim 1000$  km/s) and intense fluxes of solar energetic particles. We  
69 speculated that anomalous dynamics of the magnetosphere could be well described by the models if  
70 the He abundance in the solar wind was assumed to be  $>20\%$ , which is well appropriate for erupting  
71 filaments and which is in agreement with the upper 27% threshold for the He/H ratio obtained from  
72 Cluster measurements.

73

74

75 *Keywords:* erupting filament, geomagnetic storm, magnetosphere boundary layers, ring current decay

76

## 77 **1. Introduction**

78 During recent years, great attention was paid to events of extreme magnetospheric disturbances  
79 [Tsurutani *et al.*, 2003; Gopalswamy *et al.*, 2005; Baker *et al.*, 2013]. Those unusual events could be  
80 characterized not only by extremely strong *Dst* variations but also by extremely small size of the  
81 magnetosphere during strong or even moderate magnetic storms [Vaisberg and Zastenker, 1976; Lu  
82 *et al.*, 1998; Dmitriev *et al.*, 2005a].

83 The shrinking of the dayside magnetosphere can be caused either by erosion under southward  
84 orientation of the interplanetary magnetic field (IMF) or by an enhancement of the solar wind  
85 dynamic pressure [Chapman and Ferraro, 1931; Spreiter *et al.*, 1966; Fairfield, 1971; Gosling *et al.*,  
86 1982]. The effect of southward IMF results in saturation that limits the magnetospheric shrinking  
87 [e.g., Suvorova *et al.*, 2005; Dmitriev and Suvorova, 2012]. The solar wind dynamic pressure (*Pd*)  
88 can achieve very high magnitudes of ~100 nPa that cause very strong compression of the whole  
89 magnetosphere such that geosynchronous satellites are located temporarily in the magnetosheath or  
90 even in the interplanetary medium.

91 Table 1 presents a list of such extreme events when the bow shock and magnetopause were situated  
92 inside geosynchronous orbit, i.e. at geocentric distances below 6.6 Earth's radii (*Re*). Most of the  
93 events were accompanied by northward or alternating IMF. Hence, the extremely small size of the  
94 magnetosphere is mainly caused by abnormally high *Pd* of several tens on nPa. Very high pressures  
95 are produced by fast and dense solar wind plasma streams, which are characterized by velocities  $V >$   
96 700 km/s and densities *D* of several tens of particles per cc.

97 Such extreme conditions in the solar wind are developed either in strongly compressed sheath regions  
98 downstream of fast interplanetary shocks preceding interplanetary coronal mass ejecta (ICME) or  
99 inside so-called erupting filaments, which follow ICME and carry out chromospheric material ejected  
100 during solar flares [e.g., Schwenn, 1983; Crooker *et al.*, 2000; Foullon *et al.*, 2007; Chen, 2011]. The  
101 erupting filaments are characterized by significant helium abundance, which substantially contributes  
102 to *Pd* [Gosling *et al.*, 1980; Borrini *et al.*, 1982].

103 In Table 1, one can see that two events of very high  $Pd$  occurred during storm onset. Apparently, they  
104 were related to strong compression in the interplanetary sheath region. Other three events of extreme  
105  $Pd$  were observed on the recovery phase and they might be related to erupting filaments. It was well  
106 established that the great pressure enhancement of  $\sim 90$  nPa at 19 UT on 21 January 2005 was  
107 produced by an erupting filament [Foullon *et al.*, 2007]. Burlaga *et al.* [1998] also reported a very  
108 high-density ( $D > 185$  cm<sup>-3</sup>) region of prominence material from erupting filament with great He  
109 abundance at the rear of the magnetic cloud during the January 11, 1997 magnetic storm. However in  
110 the latter event, the total solar wind dynamic pressure did not exceed 70 nPa because of a relatively  
111 low solar wind speed,  $V \sim 400$  km/s.

112 In contrast to other events, the extreme  $Pd$  enhancement on 21 January 2005 occurred during the  
113 main phase of the magnetic storm. The strong compression was accompanied by unusual dynamics of  
114 the magnetosphere. The Double Star TC-1 satellite crossed the bow shock and entered the upstream  
115 solar wind in the dusk region at a geocentric distance of 8.5 Re from 1853 to 1907 UT [Dandouras *et*  
116 *al.*, 2009]. The very close approach of the flank bow shock to the Earth corresponds to a very small  
117 distance (much less than 6.6 Re) to the subsolar magnetopause. Du *et al.* [2008] reported that the  
118 storm on 21-22 January 2005 was highly anomalous because the storm main phase developed during  
119 northward IMF.

120 On the other hand, Kuznetsova and Laptukhov [2011] and Troshichev *et al.* [2011a,b] regarded the  
121 storm on 21-22 January 2005 as a usual phenomenon since it occurred under the influence of a large  
122 interplanetary electric field  $Em$ . The unusual  $Dst$  dynamics was explained by a great enhancement of  
123 the geoeffective  $Em$  with the initial input from the southward IMF  $Bz$  and the succeeding input from  
124 the azimuthal IMF  $By$  component against the background of the very high solar wind speed ( $V_{sw} >$   
125 800 km/s). In addition, McKenna-Lawlor *et al.* [2010] studied the ring current dynamics and  
126 demonstrated a good correspondence between magnetic field prediction by the Tsyganenko and  
127 Sitnov [2005] model and observations of energetic neutral atoms in the beginning of the storm from  
128 1700 to 1900 UT. During that time, the moderate but extended response of the magnetosphere to the

129 strong disturbance was explained by a long-duration evolution in the orientation of  $B_z$  under  
130 conditions of enhanced plasma sheet density.

131 In the present study, we focus mainly on the extremely strong enhancement of the solar wind  
132 dynamic pressure from 19 to 22 UT on 21 January 2005. We show an anomalous response of the  
133 magnetosphere to the extremely high pressure such that the existing models fail to predict the  
134 magnetospheric dynamics even under northward IMF. Heliospheric and geomagnetic conditions are  
135 presented in Section 2. The size of the magnetosphere is investigated in Section 3. Dynamics of  
136 radiation belt is studied in Section 4. The results are discussed in Section 5. Section 6 is Conclusions.

137

## 138 **2. Heliospheric and geomagnetic conditions**

139

140 The magnetic storm on 21 January 2005 was caused by an ICME generated by the X7.1/3B solar  
141 flare in the north-western quadrant of the solar disk (N14W61) that occurred at ~0640 UT on 20  
142 January 2005 [Foullon *et al.*, 2007]. The flare produced one of the most intense fluxes of relativistic  
143 solar energetic particles (SEP) [Belov *et al.*, 2005; Kuznetsov *et al.*, 2005]. Very intensive fluxes of  
144 high-energy SEPs resulted in radiation effects in space instruments that lead to distortion of the space  
145 data [e.g., Dmitriev *et al.*, 2005b].

146 Heliospheric and geomagnetic conditions during the storm on 21 January 2005 are shown in Figure 1.

147 The storm started from a sudden commencement observed at 1710 UT when a strong interplanetary  
148 shock (IS) pushed the magnetosphere. At the shock, the solar wind velocity enhanced up to ~900  
149 km/s. The shock accelerated protons with energies up to 30 MeV as measured by GOES-10. The  
150 peak flux of >30 MeV protons was  $\sim 25 \text{ (cm}^2 \text{ s sr)}^{-1}$ . Such conditions were close to the threshold of 50  
151  $\text{(cm}^2 \text{ s sr)}^{-1}$  and  $V \sim 1000 \text{ km/s}$ , which was reported for the plasma data distortion at SWEPAM  
152 instrument of the ACE upstream monitor [e.g., Dmitriev *et al.*, 2005b]. Hence, we have to consider  
153 plasma data from the ACE and other upstream monitors very carefully.

154 High-resolution ( $< 1$  min) solar wind plasma data were acquired from the ACE/SWEPAM  
155 instrument. We also use summary plasma parameters such as density, velocity and temperature  
156 provided by the Cluster Hot Ion Analyzer (HIA) instruments from all probes, and densities of low-  
157 energy He and protons measured by Composition and Distribution Function analyzer (CODIF)  
158 instrument onboard Cluster C4(Tango) [Rème *et al.*, 2001]. IMF data were obtained from the  
159 ACE/MAG instrument and the Cluster C3(Samba) flux gate magnetometer (FGM) [Balogh *et al.*,  
160 2001]. Note that magnetic measurements of other Cluster probes were very similar to those provided  
161 by Samba. During the storm, the Cluster satellites were located in the interplanetary medium at  $X_{\text{GSM}}$   
162  $\sim 15$  Re,  $Y_{\text{GSM}} \sim 12$  Re,  $Z_{\text{GSM}} \sim -3$  Re, i.e. in the postnoon sector. The time profiles of the ACE and  
163 Cluster data are shifted using the time lags for solar wind propagation to the Earth ( $\sim 1$  min and  
164 around 30 min, respectively).

165 As one can see in Figure 1, the plasma and magnetic data from the ACE and Cluster satellites are in  
166 very good agreement, excepting profiles of  $D$ , He/H and IMF  $B_x$  during the interval from  $\sim 1900$  to  
167 2130 UT. It seems that the relatively low He contribution detected by ACE could result from  
168 malfunction of the Composition Aperture telescope of the SWEPAM instrument in the very fast solar  
169 wind stream ( $V \sim 1000$  km/s) and under enhanced fluxes of high-energy SEP as it happened during  
170 29–31 October event [Dmitriev *et al.*, 2005a]. A strong difference in  $B_x$  is revealed during time  
171 interval from  $\sim 1945$  to 2100 UT when ACE observed large negative  $B_x$  while Cluster observed large  
172 positive one. Foullon *et al.*, [2007] reported that the solar wind structure with negative  $B_x$  was also  
173 observed by the Wind and Geotail satellites located as ACE in the dawn hemisphere. The authors  
174 explained the strong difference in  $B_x$  profiles by a tilted and curved current sheet whose center of  
175 curvature was in the north-dawn sector while Cluster was located in the dusk sector. In other words,  
176 Cluster observed only a part of the solar wind affecting the magnetosphere in the postnoon region.  
177 The prenoon and dawnside magnetosphere was affected by a different solar wind structure.  
178 Cluster and ACE observed different magnetic fields and solar wind density  $D$ . Strong electric  
179 currents should exist in the space between them. Those electric currents and dense plasma stroked on

180 the magnetosphere around this time and partially penetrated inside. The specific and unusual case  
 181 was that the solar wind and IMF parameters were highly inhomogeneous on the scale size of the  
 182 magnetosphere and distorted its structure.

183 Therefore, the total solar wind dynamic pressure  $Pd$  can be calculated separately for the dawn (ACE)  
 184 and dusk (Cluster) sectors using the following expression:

$$185 \quad Pd = 1.67 \cdot 10^{-6} DV^2 \left(1 + 4 \frac{He}{H}\right), \quad (1)$$

186 where  $D$  and  $V$  were measured by ACE or Cluster, and helium contribution  $He/H$  was acquired from  
 187 the Cluster C4 data. As one can see in Figure 1, the resultant  $Pd$  are quite different within the interval  
 188 from  $\sim 1900$  to  $\sim 2200$  UT. The solar wind dynamic pressure is further used for correction of the  $Dst$   
 189 index in order to eliminate the effect of Chapman-Ferraro current at the magnetopause and reveal the  
 190 contribution of inner magnetospheric currents. We apply an expression derived by *O'Brien and*  
 191 *McPherron* [2002]:

$$192 \quad Dst^* = Dst - 8.6 \sqrt{S(\psi)} (\sqrt{Pd} - 1.5), \quad (2)$$

$$193 \quad \text{where } S(\psi) = \frac{1.15}{(1 + 3 \cos^2 \psi)^{2/3}}$$

194 Here  $Dst$  and  $Pd$  are expressed in nT and nPa, respectively, and  $\psi$  is subsolar magnetic colatitude.

195 In the beginning of the storm, from 1712 to 1846 UT, the dynamics of  $Dst$  and  $Dst^*$  indices can be  
 196 well described as a function of  $Bz$  (actually  $Ey = V \cdot Bz$ ) and  $Pd$ . From 1710 to 1722 UT,  $Dst$  increased  
 197 abruptly from  $-20$  to  $\sim 60$  nT due to an enhancement of  $Pd$  from a few to  $\sim 20$  nPa. Prominent  
 198 decreases of  $Dst$  and  $Dst^*$  correspond to intensification of the ring current during intervals of  
 199 southward IMF from  $\sim 1720$  to 1750 UT and from 1820 to 1840 UT. *McKenna-Lawlor et al.* [2010]  
 200 reported that the ring current was well developed by 1900 UT. An increase of  $Dst$  and  $Dst^*$  from  
 201 1750 to 1820 UT was caused by recovery of the ring current under northward IMF.

202 We also use empirical models in order to predict the storm-time  $Dst$  variation. Figure 2 shows a  
 203 comparison of the observed hourly averaged  $Dst$  variation with predictions by Wang model [*Wang et al.*  
 204 *et al.*, 2003], MO model [*McPherron and O'Brien*, 2001], OM model [*O'Brien and McPherron*, 2000],



205 FL Model [Fenrich and Luhmann, 1998], and Burton model [Burton et al., 1975]. Note that in the  
206 *Dst* (ring current) prediction model, the injection only occurs when IMF is southward, and the decay  
207 rate may be dependent on  $V$ ,  $B_y$ ,  $B_z$  and  $Pd$  for some models. All models are optimized based on a  
208 number of historical data. As one can see in Figure 2, all the models predict *Dst* quite well in the  
209 beginning of the storm from 1700 to 1900 UT. However after 1900 UT, all the models fail and  
210 predict a recovery phase while the *Dst* decreases sharply on several tens of nT. The decrease could  
211 not be predicted by any model because IMF was mainly northward during that time.

212 In Figure 1 one can see that most prominent difference between *Dst* and *Dst\** is revealed from ~1900  
213 to 2100 UT. During that time, *Dst* was decreasing by ~85 nT from ~45 nT to ~ -40 nT, while *Dst\**  
214 corrected by the ACE pressure was almost constant and varying around -70 nT. Hence, the dynamics  
215 of *Dst* can be well attributed to a decrease of  $Pd$  from ~120 to 20 nPa. However, behavior of *Dst\** is  
216 anomalous because under positive  $B_z$ , the ring current should decay and, thus, *Dst\** should increase.  
217 It looks like the ring current did not decay from ~1900 to 2100 UT.

218 From 2055 to 2115 UT, *Dst\** has decreased from ~ -70 to ~ -130 nT. The strong decrease of *Dst\** is  
219 hard to explain by short intervals with negative  $B_z$  of small magnitude as well as by variations in  $Pd$ .  
220 From 2115 to 2400 UT, IMF remained northward and  $Pd$  was varying about 30 nPa. During this  
221 time, *Dst\** started to increase that indicates to decay of the ring current. However, this decay was  
222 abnormally slow.

223

### 224 **3. Geosynchronous crossings of the magnetopause and bow shock**

225

226 We determine the size of the magnetosphere using observations and modeling of the magnetopause  
227 and bow shock by geosynchronous satellites. The magnetopause is modeled by an empirical model of  
228 Kuznetsov and Suvorova [Kuznetsov and Suvorova, 1998; Suvorova et al., 1999] (hereafter KS98  
229 model), which has demonstrated very good capabilities for prediction of the dayside magnetopause in  
230 very wide dynamic range and enables predicting a storm-time dawn-dusk asymmetry [Dmitriev et al.,

231 2005a; 2011]. Note that KS98 model demonstrates best capabilities in prediction of the strongly  
232 compressed magnetopause under northward IMF [*Suvorova et al.*, 2005]. We also use an empirical  
233 model by *Dmitriev et al.* [2011] predicting the solar wind pressure  $P_{gmc}$  required for  
234 geosynchronous magnetopause crossing at a given location. Namely, if  $P_{gmc}$  is lower (higher) than  
235  $P_d$  then a geosynchronous satellite is expected to be located in the magnetosheath (magnetosphere).  
236 This model is based on advanced set of geosynchronous magnetopause crossings observed in an  
237 extremely wide range of IMF  $B_z$  from  $-30$  to  $30$  nT.

238 The bow shock is modeled by *Verigin et al.* [2001] model (hereafter BSV model) and by *Chao et al.*  
239 [2002] model (hereafter BSC model). Note that the BSV model depends on the size and shape of the  
240 dayside magnetopause, which is calculated by the KS98 model [e.g., *Dmitriev et al.*, 2003]. The BSC  
241 model does not depend on modeling of the magnetopause. The BSV and BSC models demonstrated  
242 quite high capabilities for prediction of the bow shock in the previous statistical studies [*Dmitriev et*  
243 *al.*, 2003].

244 We also use results of global MHD modeling of the magnetosphere performed by SWMF/BATS-R-  
245 US code with Fok ring current (version v20110131) provided by the Community Coordinated  
246 Modeling Center (*Alexei\_Dmitriev\_072512\_1*). The model is driven by upstream solar wind and  
247 IMF data acquired from the ACE satellite within the time interval from 1630 to 2400 UT on 21  
248 January 2005. The code allows tracing of geosynchronous and other satellites to obtain model values  
249 of magnetic field and plasma parameters along the orbit.

250 Figure 3 shows the location of GOES-10, GOES-12, LANL-1990, LANL-1994, LANL-1997, Cluster  
251 and Double Star TC-1 satellites at  $\sim 1850$  UT on 21 January 2005. The profiles of magnetopause and  
252 bow shock are calculated, respectively, by the KS98 and BSV models for extreme solar wind  
253 conditions: Alfvén Mach number  $Ma = 8$ , sonic Mach number  $Ms = 12$ ,  $B_z = -20$  nT,  $P_d = 90$  nPa. As  
254 one can see, the subsolar bow shock and practically the whole dayside magnetopause are located  
255 inside geosynchronous orbit such that all the geosynchronous satellite should be located either in the  
256 magnetosheath or even in the upstream solar wind.

257 Figure 4 shows GOES-10 and GOES-12 observations of the magnetic field from 17 to 24 UT on 21  
258 January 2005. The magnetopause crossed GOES-12 at local noon right in the beginning of the storm  
259 at 1712 UT. Until 1840 UT, GOES-12 was located in the magnetosheath where  $B_x$ ,  $B_y$  and  $B_z$   
260 components of the magnetic field were strongly magnified and correlated well with the corresponding  
261 IMF components observed by Cluster. At the same time, GOES-10 was located in the dawn –  
262 prenoon sector and encountered with the magnetosheath from 1736 UT to 1750 UT and from 1821 to  
263 1846 UT.

264 At 1846 UT, both GOES-10, located in the prenoon sector, and GOES-12, located in the postnoon  
265 sector, crossed the bow shock and came into the interplanetary medium where they observed  
266 practically the same magnetic field as Cluster. The satellites situated upstream of the bow shock  
267 during ~2 hours and returned to the magnetosheath at 2035 and 2010 UT, respectively. That long  
268 duration of the interplanetary interval is really outstanding for the geosynchronous satellites.

269 During the interplanetary interval, the GOES satellites observed positive IMF  $B_x$ , which was  
270 consistent with the Cluster observations. Note that at 1945 UT, ACE observed a reversal of the IMF  
271  $B_x$  component (see Figure 1). Hence, it is reasonable to suggest that Cluster observed the solar wind  
272 and IMF conditions, which did affect most part of the dayside magnetosphere from the prenoon  
273 (GOES-10) to dusk (GOES-12) sector.

274 In Figure 4 one can see that from 1712 to 1846 UT, the magnetopause crossings and magnetosheath  
275 intervals are well predicted by KS98 and MHD models both in prenoon and postnoon sectors. The  
276 dynamics of modeled pressure  $P_{gmc}$  is also in good agreement with the observations: time intervals  
277 of  $P_{gmc} < P_d$  correspond well to the magnetosheath intervals observed by the GOES satellites.

278 However, the interplanetary interval from 1846 to 2035 UT cannot be completely predicted by the  
279 models. The BSV model predicted only a brief solar wind encounter from 1846 to 1855 UT when the  
280 IMF turned southward. The BSC model, based on either ACE or Cluster dynamic pressure, cannot  
281 predict any bow shock crossings. The MHD model predicts strong variations of high-amplitude

282 magnetic field that rather typical to the magnetosheath than to the interplanetary magnetic field.  
283 Hence, the models fail to predict the bow shock location for the present event.  
284 Additional inconsistencies can be found during the GOES-12 magnetosphere encounter at 2130 UT  
285 when the solar wind dynamic pressure was decreasing gradually. The magnetopause crossing was  
286 observed under decreasing  $Pd$ , which was already much lower than  $P_{gmc}$  for  $\sim 20$  min. The KS98  
287 model also predicted the magnetopause crossing much earlier (at  $\sim 2105$  UT) than actual one.  
288 However, the magnetospheric encounter by GOES-10 at 2340 UT was predicted by KS98 quite  
289 precisely.

290 In Figure 5, we show magnetosheath interval observed by LANL-1997 from 1912 to 2400 UT.  
291 LANL satellites do not detect magnetic field but they measure plasma characteristics. For this case,  
292 the magnetopause crossings are identified by using so-called a ratio of ion density to temperature (RI)  
293 and of electron density to temperature (RE) (see details in *Suvorova et al.*, [2005]). In the hot  
294 magnetospheric cavity, the ratios RI and RE are small ( $< 1$ ) while they are high ( $\sim 100$ ) in the dense  
295 and hot magnetosheath. Note that the actual threshold can become lower due to a radiation effect of  
296 SEP [*Dmitriev et al.*, 2005a]. For the present case we use the threshold of  $RI \sim 10$ .

297 At 1912 UT, LANL-1997 crossed the magnetopause and encountered with the magnetosheath at very  
298 early local morning ( $\sim 0530$  MLT). The magnetopause crossing by LANL-1997 was in good  
299 agreement with the value of  $P_{gmc}$ , which was smaller than  $Pd$  measured by Cluster. However, the  
300 KS98 model could not completely predict the magnetosheath interval. The model overestimated the  
301 magnetopause distance from 1912 to  $\sim 2100$  UT. Hence, we can conclude that the KS98 model fails to  
302 predict the magnetopause crossings during time interval from 1912 to 2130 UT both in the dawn and  
303 dusk sectors. It seems that higher  $Pd$  is required for the KS98 model in order to give a correct  
304 prediction for GOES-12 and LANL-1997.

305 From the observations, we can determine that in the noon region, the magnetopause was located  
306 inside geosynchronous orbit from 1712 on 2400 UT. The minimal distance to the magnetopause of  $\sim 3$   
307  $R_e$  was predicted by KS98 model at  $\sim 1850$  UT. From 1846 to 2035 UT, geosynchronous orbit in the

308 noon region was located upstream of the bow shock and practically whole dayside magnetopause  
309 came inside geosynchronous orbit. We can approximately estimate the magnetopause distance during  
310 the interplanetary interval taking into account an average ratio of 1.3 for the distances to the subsolar  
311 bow shock and magnetopause [*Spreiter et al.*, 1966]. For the bow shock distance of 6.6 Re we obtain  
312 the magnetopause distance of  $\sim 5$  Re. Hence during almost 2 hours from 1846 to 2035 UT 21 January  
313 2005, the magnetosphere was extremely compressed such that the distance to the subsolar  
314 magnetopause was less than 5 Re.

315

#### 316 **4. Dynamics of the ring current and radiation belt**

317

318 Extremely strong long-lasting compression of the magnetosphere should affect the radiation belt and  
319 dynamics of the ring current. The fast and dramatic magnetosphere shrinking from 1846 to 1855  
320 followed by an  $\sim 2$ -hour decrease of the compression should violate the third adiabatic invariant of  
321 protons with energies from tens of keV to a few MeV in the outer magnetosphere at drift shells  $L > 4$ .  
322 Therefore from 1846 to 2035 UT 21 January 2005, the radiation belt and ring current should be  
323 significantly modified and restricted by the upper boundary located at  $L \sim 5$ . Here we use low-orbit  
324 high-inclination satellites CORONAS-F and POES for studying the radiation belt and ring current  
325 dynamics.

326 Figure 6 shows temporal variations of pitch-angle anisotropy for the protons with energies of tens of  
327 keV observed by POES-17 near the noon-midnight meridian on 21 January 2005 at  $L \sim 5$   
328 corresponding to the outer magnetosphere. The anisotropy is calculated as a ratio between trapped  
329 proton fluxes with pitch angles  $\alpha \sim 90^\circ$ , i.e. perpendicular to the magnetic field line, to precipitating  
330 ones with  $\alpha \sim 0^\circ$ . Before the magnetic storm, the satellite observed mostly trapped energetic protons  
331 gyrating near their mirror points such that the ratio was varying around 100. During magnetospheric  
332 compression at  $\sim 18$  UT and especially from  $\sim 1900$  to  $\sim 2200$  UT, the anisotropy was mainly  $\sim 1$  and  
333 even less than 1 that corresponded to a diminishing the trapped proton population in the outer  
334 magnetosphere.

335 Dynamics of proton fluxes observed by POES-17 satellite near the noon-midnight meridian on 21–22  
336 January 2005 is shown in Figure 7. Before the storm at 1700 UT, integral fluxes of low-energy ( $> 30$   
337 keV) protons had a maximum of up to  $\sim 10^9$  ( $\text{cm}^2 \text{ s sr}^{-1}$ ) at  $L = 4$ . During the storm development, the  
338 fluxes were substantially increasing mainly in the inner magnetosphere at  $L < 4$  such that at 2100 UT,  
339 the fluxes of  $>30$  keV,  $>80$  keV and  $> 200$  keV protons enhanced by almost two orders of magnitude  
340 and peaked at  $L = 2$  and 3. In contrast, the proton fluxes have diminished in the outer magnetosphere  
341 at  $L = 4$  and 5. Such dynamics corresponds to fast transport of the ring current particles into the inner  
342 regions and losses of radiation belt particles at  $L > 4$  (magnetopause shadowing) due to a strong and  
343 long-lasting compression of the magnetosphere.

344 CORONAS-F satellite observed a similar dynamics of energetic protons (1–5 MeV) as shown in  
345 Figure 8. From  $\sim 18$  to  $\sim 22$  UT, the fluxes in the inner magnetosphere increased up to 3 orders of  
346 magnitudes. Most significant proton enhancement can be revealed in the range of  $L$ -shells from 2 to  
347 4. It is important to note that the proton fluxes at  $L = 2$ –3 have diminished very fast after 23 UT that  
348 is caused by very intense particle losses in the inner magnetosphere. Note that at  $L = 3$ –5, the particle  
349 fluxes remained high and were decreasing gradually during the rest of the storm.

350 From observation of the low-energy protons we found that the extreme compression of the  
351 magnetosphere from  $\sim 1850$  to  $\sim 2100$  UT on 21 January 2005 was accompanied by anomalous  
352 transport of the particles from the outer to the inner regions. The outer magnetosphere at  $L > 5$  was  
353 pushed inward during the extreme compression. The particles from the radiation belt and ring current  
354 were accumulated in the inner magnetosphere at  $L < 4$ . The dynamics of the proton fluxes in the inner  
355 magnetosphere did not reveal substantial losses until the end of compression.

356

## 357 **5. Discussion**

358

359 From analysis of the geomagnetic storm on 21 January 2005, we have found that the storm can be  
360 divided in two parts accompanied by essentially different solar wind dynamic pressures. The

361 beginning of the storm lasted from 1712 to 1846 UT under  $Pd < 20$  nPa. During this phase, the  
362 dynamics of the magnetospheric boundaries, magnetopause and bow shock, as well as the ring  
363 current are well predicted by empirical and first-principle models. The situation changed dramatically  
364 after 1846 UT when an extremely high solar wind pressure and strong southward IMF (at 1846–1855  
365 UT) smashed out the outer magnetosphere such that a part of geosynchronous orbit at 10 to 14 MLT  
366 occurred inside the upstream solar wind for almost 2 hours.

367 We can make indirect estimation of the subsolar distances for the extremely compressed  
368 magnetopause and bow shock on the base of the fact that from 1853 to 1907 UT, Double Star TC-1  
369 entered into the upstream solar wind [*Dandouras et al.*, 2009]. We use various models [see *Dmitriev*  
370 *et al.*, 2003 for details] in order to calculate the bow shock subsolar distances  $R_s$  when Double Star  
371 TC-1 crosses the bow shock at GSM location ( $X = 1.3$ ,  $Y = 7.4$ ,  $Z = 4.0$  Re) under strong southward  
372 IMF ( $B_z = -23$  nT). We also use a model shape of the bow shock proposed by *Cairns et al.* [1995].  
373 Table 2 shows the resultant  $R_s$  and  $Pd$  required for the Double Star TC-1 crossing of the bow shock.  
374 Only models by *Russell and Petrinec* [1996], BSV and BSC enable to predict the crossing for the  
375 given solar wind conditions. Other models overestimate the bow shock distance substantially. From  
376 Table 2 we find that from 1853 to 1907 UT, the subsolar bow shock was located below 5.2 Re and,  
377 thus, the magnetopause nose distance was smaller than 4 Re. Note that actual distances to the bow  
378 shock and magnetopause could be much smaller.

379 During the period of extreme magnetospheric compression, the behavior of the magnetosphere  
380 became very unusual: all the models failed to predict the magnetospheric dynamics. Namely, no  
381 model could predict the extremely small size of the magnetosphere: bow shock location at 6.6 Re for  
382 ~2 hours and magnetosheath encounter at very early local time of ~0530 MLT. The empirical models  
383 could not predict the anomalous increase of negative  $Dst$  variation, or storm main phase, observed  
384 under northward IMF that meant an unusual intensification of the “non-decaying” ring current. It  
385 seems that the models may be not workable for extreme condition such as extremely compressed  
386 magnetosphere or steady northward IMF. In addition, the  $B_y$  component of IMF is large for this

387 event. There may exist partial component magnetic reconnection at the subsolar point when there is  
 388  $B_y$  component. This may also contribute to injection of ring current particles as proposed by  
 389 *Kuznetsova and Laptukhov* [2011] and *Troshichev et al.* [2011a,b].  
 390 *Du et al.* [2008] proposed two possible mechanisms to explain the anomalous behavior of  $Dst$ . The  
 391 first one consists in a lengthy storage of solar wind energy in the magnetotail and delayed release into  
 392 the ring current. However, we do not find any particle injections in the outer magnetosphere during  
 393 time interval from 1999 to 2035 UT. Instead, in the night and evening sectors, we observe weaker  
 394 fluxes at  $L = 4-5$  than those at  $L = 3-4$ . Decreases of  $Dst$  after 2035 UT might be caused by  
 395 intensification of the substorm activity observed under strong compression in the sub-auroral zone  
 396 [*Lazutin and Kuznetsov*, 2008; *Lazutin et al.*, 2010]. The substorm activity was caused by  
 397 enhancements of the solar wind dynamic pressure and southward IMF turnings observed by the  
 398 satellites ACE, Cluster (See Figure 1) and GOES-10 (see Figure 4).  
 399 The second mechanism proposed by *Du et al.* [2008] that during the storm, the plasma sheet may be  
 400 close to the Earth, resulting in a large contribution of the tail current to the  $Dst$  index. However, the  
 401 inner part of tail current, being strong and close to the Earth in the beginning of compression, should  
 402 move out and become weaker within  $\sim 10$  minutes after a decrease of the solar wind dynamic pressure  
 403 and northward IMF turning [*Borovsky et al.*, 1998; *Tsyganenko*, 2000]. The magnetic effect of tail  
 404 current was found to be dominant in the  $Dst$  variation during moderate magnetic storms with  $Dst_{\min} >$   
 405  $-100$  nT [*Ganushkina et al.*, 2010]. As shown by *Tsyganenko* [2000], the best driving parameters for  
 406 the tail current are  $\lg(Pd)$  and a complex function of the solar wind velocity  $V$ , IMF transversal  
 407 component  $B_{\perp} = (B_y^2 + B_z^2)^{1/2}$  and clock angle  $\theta$ :  $\varepsilon = V \cdot \sin^3(\theta/2) \times (B_{\perp}/B_c)^2 / (1 + B_{\perp}/B_c)$ , where  $B_c = 40$   
 408 nT. In Figure 9 one can see that from 1845 to  $\sim 1900$  UT, both  $\varepsilon$  and  $Pd$  increase dramatically and,  
 409 thus, the tail current contribution to negative  $Dst$  was significant at that time. However, after 1900  
 410 UT, both  $\varepsilon$  and  $Pd$  decrease rapidly that indicates to diminishing tail current. Hence, the tail current  
 411 cannot explain the “non-recovering”  $Dst$ .



412 Another possible source of the ring current might be solar energetic particles [*Hudson et al.*, 1997;  
413 2004; *Richard et al.*, 2009]. It has been shown that SEP penetration is effective during strong  
414 compression of the magnetosphere by interplanetary shocks. However, the SEP flux during the shock  
415 passage at ~1845 UT was not very strong ( $\sim 10^3 \text{ (cm}^2 \text{ s sr)}^{-1}$  for  $>1 \text{ MeV}$  protons as shown in Figure  
416 1) such that the SEP protons could contribute only a little portion of the ring current. Further after the  
417 compression, trapped and quasi-trapped particles are lost by motion through the magnetopause and  
418 by precipitation. This should result in a gradual decrease of the particle fluxes and, thus, a decrease of  
419 their contribution into the ring current. Hence, we can neglect the effect of SEP penetration.

420 The mechanisms proposed cannot also explain the observations of both extreme and long-lasting  
421 magnetopause compression. The negative magnetic effect to the subsolar geomagnetic field (if any)  
422 should diminish with decreasing  $Pd$  and the magnetosphere should expand as predicted by the models  
423 during time interval from ~19 to 21 UT on 21 January. However, we did not find this expansion in  
424 both the bow shock location and radiation belt profile. Instead, the standoff magnetopause was below  
425 5  $R_e$  during that time.

426 Here we have to remind that the solar wind plasma of very high density was originated from an  
427 erupting filament [*Foullon et al.*, 2007], which usually contains a significant portion of He. *Sharma et*  
428 *al.* [2013] reported very large He to proton ratio of  $>20\%$  in the filament plasma observed by  
429 ACE/SWICS on 7–8 January 2005. It is important to note that those days were not accompanied  
430 either by enhanced SEP fluxes or by very fast solar wind and, hence, the Composition Aperture  
431 telescope onboard ACE was operating safely. In contrast during the 21 January storm, the SEP fluxes  
432 were intense and the solar wind speed was high (see Figure 1) such that both ACE and Cluster  
433 detectors suffered from the radiation impact [*Foullon et al.*, 2007]. The two satellites measured very  
434 similar proton density but very different He to proton ratio. Hence, it is reasonable to assume that the  
435 experimental data on the He/H ratio are not reliable and He contribution can be underestimated.

436 Figure 10 demonstrates Cluster plasma data from the more recent calibrations of the CIS team  
437 (communicated to us by the anonymous Reviewer of this paper). It is well known that CODIF is a

438 time-of-flight ion mass spectrometer, designed mainly for magnetospheric ions, and it can thus be  
439 saturated under intense solar wind fluxes as those encountered here (*Rème et al., 2001*; and *CIS User*  
440 *Guide*, available at the CAA: [http://caa.estec.esa.int/caa/ug\\_cr\\_icd.xml](http://caa.estec.esa.int/caa/ug_cr_icd.xml)). HIA, in the low-sensitivity  
441 side operation (as was the case here), can instead handle very intense fluxes without this saturation  
442 problem. This is evident from Figure 10 where after 1844 UT, HIA measured a jump of the solar  
443 wind density up to  $\sim 57 \text{ cm}^{-3}$ , whereas CODIF at this time showed no increase of the proton density,  
444 and showed even a small “decrease”, typical for saturation conditions. The total ion density is thus  
445 supplied by HIA. CODIF, however, can still give a rough measure of the  $\text{He}^{++}$  contribution. As  
446 shown in Figure 1, the “measured”, under saturation conditions, proton density was  $\sim 8.5 \text{ cm}^{-3}$ ,  
447 whereas at the same time the “measured”  $\text{He}^{++}$  density was  $\sim 2.3 \text{ cm}^{-3}$ . This gives a  $\text{He}^{++}$  to proton  
448 ratio of  $\sim 27\%$ . Note that this is an upper limit, because the proton channel suffers from a stronger  
449 saturation than the  $\text{He}^{++}$  channel (due to the much higher proton fluxes, as shown in Figure 10,  
450 indicating stronger saturation signatures). The actual  $\text{He}^{++}$  to proton ratio is thus clearly less than 27%  
451 but above the  $\sim 8\%$  shown as the “observed” CODIF He/H ratio in Figure 1.

452 Therefore the discrepancies between the observations and model predictions can be originated from  
453 “insufficiently strong” solar wind dynamic pressure because of underestimation of the He  
454 contribution. Using empirical models of the bow shock and magnetopause, we can estimate the He  
455 contribution and  $Pd$  required for observed magnetopause and bow shock crossings. In Figure 9, we  
456 show predictions of the empirical models for a “synthetic”  $Pd$  derived from the Cluster HIA  
457 measurements but with 4-time magnification of the He contribution acquired from original  
458 Tango/CODIF plasma measurements (see Figure 1).

459 The “synthetic”  $Pd$  is very close to the observed one in the beginning of the storm because of very  
460 low original He content at that time. During the extreme compression, the He/H ratio increased up to  
461  $\sim 30\%$  and, thus, the “synthetic” solar wind dynamic pressure enhanced up to 200 nPa. As one can see  
462 in Figure 9, the magnitude and dynamics of “synthetic”  $Pd$  allows successful predicting the  
463 interplanetary interval from 1846 to 2035 UT. Moreover, the profile of pressure corrected  $Dst^*$

464 becomes not so much anomalous. Namely, a decrease from 1846 to ~1920 UT can be attributed to  
465 intensification of the ring current due to the southward IMF turnings observed at that time by both  
466 ACE and Cluster satellites.

467 Helium contribution of ~30% shown in Figure 9 is slightly higher than 27% upper threshold obtained  
468 from Cluster measurements. The 10% difference leads to ~5% decrease in the solar wind dynamic  
469 pressure from 195 to 184 nT. This decrease is small and does not affect much the results obtained  
470 above. Actual value of the He/H ratio could be even smaller than 27% leading to the decrease in  $Pd$   
471 of ~ 20% and even 30%. However in the KS98 model, the size of magnetopause depends on the  
472 dynamic pressure as  $R_s \sim (Pd)^{-1/5.2}$  and the pressure correction of  $Dst$  depends on  $Pd^{1/2}$ . Hence, the  
473 decrease of  $Pd$  gives the result lying within the model errors, especially in the range of extrapolation.  
474 Much more important problem, especially for the  $Dst$  correction, is temporal dynamics of the He/H  
475 ratio, which is hard to derive from the experimental data.

476 Based on the “synthetic” data we obtain that from 1920 to 2035 UT,  $Dst^*$  was varying around -100  
477 nT and did not practically decrease despite of northward IMF. This effect can be related to the  
478 dynamics of ring current during the strong magnetospheric compression. The trapped particles were  
479 moving to lower  $L$ -shells and accelerated adiabatically in a betatron mechanism, which was keeping  
480 the first two adiabatic invariants. This process enforced the ring current. The abrupt increase and long  
481 lasting decrease of magnetospheric compression of duration comparable with the drift periods of  
482 particles in the outer zone resulted in violation of the third adiabatic invariant. Hence after the  
483 extreme compression, the particles gained energy and remained at lower  $L$ -shells. This effect can be  
484 revealed in Figure 7 as a strong increase of the low-energy proton fluxes observed by POES in the  
485 inner magnetosphere at ~21 UT, i.e. in the end of the extreme compression. In contrast, there is a  
486 deficiency of protons in the outer magnetosphere.

487 Qualitative estimations of the effects of adiabatic transport and intensification of the ring current are  
488 conducted in Appendix A. We found that the low energy protons were accumulated and kept high  
489 fluxes in the inner magnetosphere at  $L < 4$  such that the total number of particles in the ring current

490 did not practically change. However, the inner magnetosphere is characterized by very intense losses  
491 of the low-energy protons in charge-exchange interactions with neutral atoms of the exosphere [see  
492 *Cornwall and Schulz, 1979; Kistler et al., 1989*]. Such losses should result in a fast decay of the ring  
493 current and formation of recovery phase with positive variation in  $Dst^*$ , which was not observed.  
494 Exosphere's density at  $L > 3.5$  varies within 20% and increases during magnetic storms [e.g.,  
495 *Østgaard et al., 2003; Bailey and Gruntman, 2013*], that promotes a decrease of lifetime of ions in  
496 the ring current. In addition, statistical studies of magnetic storms found that the decay time  
497 decreased with increasing solar wind dynamic pressure [*Wang et al., 2003*]. It was also shown that  
498 the decay time during recovery phase depends on the storm magnitude: for moderate storms with  
499  $Dst_{\min} > -125$  nT, the decay time increases with the storm magnitude [*Pudovkin et al., 1985*], while  
500 for strong magnetic storms an opposite effect was revealed [*Feldstein et al., 1984*].

501 The charge-exchange decay of the ring current and decay time dependence on the ring current  
502 location are controlled by two concurrent effects [*Kovtyukh, 2001*]: (1) the closer location of the ring  
503 current the higher exosphere's density that decrease the decay time; (2) with moving toward the  
504 Earth, ring current particles suffer betatron accelerated and if the cross-section for charge-exchange  
505 decreases with increasing energy, then the lifetime of ring current ions should increase. For the  
506 protons with energies  $E > 30$  keV, the cross-section for charge-exchange decreases fast [*Clafin,*  
507 *1970; Cornwall and Schulz, 1979; Kistler et al., 1989*] and, hence, the latter effect dominates: the  
508 decay of the ring current decreases with decreasing distance to the Earth. For oxygen ions ( $O^+$ ), the  
509 charge-exchange cross-section has a dependence on the energy much weaker than that for the protons  
510 [*Cornwall and Schulz, 1979; Kistler et al., 1989*] that results in dominance of the first effect: the  
511 decay of ring current increases with decreasing the distance to the Earth.

512 During strong magnetic storms enriched by  $O^+$  the decay time is short in the beginning of recovery  
513 phase [see *Kovtyukh, 2001* and references therein]. During weak and moderate storms, such as the  
514 event considered, the ring current is mainly contributed by protons. Hence, shifting the ring current

515 toward the Earth (as considered in details in Appendix A) results in significant increase of its  
 516 lifetime. Therefore, we can propose an effect of weak particle losses in the inner magnetosphere.  
 517 We can estimate the change of the lifetime for the protons in the maximum of ring current during its  
 518 energization and earthward shifting. The lifetime can be calculated as  $\tau = (\sigma v n_H)^{-1}$ , where  $\sigma$  is the  
 519 cross-section for charge exchange,  $v$  is velocity of protons and  $n_H$  is density of the exosphere. From  
 520 Appendix A we find that the maximum of ring current moves from  $L \sim 4.4$  to  $L \sim 3.1$  and, thus, the  
 521 exospheric density increases by  $\sim 3$  times from 200 to 600  $\text{cm}^{-3}$  [Østgaard *et al.*, 2003]. At the same  
 522 time, the protons are accelerated when move to the region with higher magnetic field. The  
 523 acceleration can be estimated as a ratio of magnetic field strength at  $L \sim 3.1$  and  $L \sim 4.4$  near  
 524 equatorial plane:  $(4.4/3.1)^3 \sim 3$ . Hence, the proton velocity increases as  $\sqrt{3} \sim 1.7$ . In the energy range  
 525 above 30 keV, the cross-section of charge-exchange for protons decreases with particle energy  $E$   
 526 approximately as  $E^{-4}$  [Claflin 1970]. If the proton energy increases by 3 times then the cross-section  
 527 decreases by  $\sim 80$  times. Therefore, the lifetime of protons increases by  $80/(1.7 \cdot 3) > 10$  times and,  
 528 thus, accelerated protons of the ring current can survive in the inner magnetosphere for a long time  
 529 and support the “non-decaying” ring current from 1920 to 2035 UT.

530 During the extreme compression, the outer magnetosphere ( $L > 5$ ) was affected by a dense and slow  
 531 plasma fluxes from the magnetosheath. The solar wind flux can be estimated as  $j_{sw} = V \times D = 940 \text{ km/s}$   
 532  $\times 50 \text{ cm}^{-3} \sim 5 \cdot 10^9 \text{ (cm}^2 \text{ s)}^{-1}$ . This flux affects a large portion of the outer magnetosphere on the  
 533 dayside during  $t \sim 2$  hours ( $\sim 7000$  s). In the magnetosheath, the solar wind ions are decelerated to  $\sim 1$   
 534 keV energies, which correspond to the cross-section for protons charge-exchange of  $\sigma \sim 2 \cdot 10^{-15} \text{ cm}^2$   
 535 [Claflin, 1970]. We can roughly estimate the relative decrease of the exospheric density as  $\sigma \cdot j_{sw} \cdot t \sim$   
 536  $7 \cdot 10^{-2}$ . Hence, almost 10% of the outer exosphere is eroded by the solar wind that results in  $\sim 10\%$   
 537 increase of the lifetime of the ring current populating the outer magnetosphere after the decrease of  
 538 solar wind pressure at  $\sim 2035$  UT. This effect might also contribute to very slow recovery of  $Dst^*$   
 539 after 2115 UT.

540 Finally, we have to emphasize that accurate pressure correction of the  $Dst$  variation is crucially  
 541 important for estimation of the ring current contribution to the storm-time magnetosphere dynamics  
 542 [e.g., Lu *et al.*, 1998]. However during most of extreme events, we can not get completely reliable

543 data on the key plasma parameters, especially proton density and He contribution, because of very  
544 fast solar wind streams and/or SEP radiation impact to the plasma instruments [*Dmitriev et al.*,  
545 2005b; *Foullon et al.*, 2007; *Russell et al.*, 2013]. Design of new space plasma instruments robust  
546 under extreme conditions should become an important issue for the future space missions.

547

## 548 **6. Conclusions**

549

550 Analysis of the solar wind conditions and dynamics of the magnetosphere and radiation belt during  
551 anomalous magnetic storm on 21 January 2005 has provided us the following findings:

552 1. The storm was unusual because it was developing under very strong solar wind dynamic pressure  
553 and/or large northward IMF such that from 1712 to 2400 UT, the noon region of geosynchronous  
554 orbit was continuously located in the magnetosheath and was exposed to the upstream solar wind  
555 during ~2 hours.

556 2. The beginning part of the storm, lasting from 1712 to 1846 UT, was typical and can be  
557 successfully predicted by the existing models of the magnetopause and ring current as well as by the  
558 global MHD simulations.

559 3. Anomalous magnetospheric dynamics, under which all the models failed, was revealed after 1846  
560 UT and related to the extremely strong dynamic pressure  $Pd > 100$  nPa produced by the dense and  
561 fast plasma of erupting filament.

562 4. During ~2 hours from 1846 to 2035 UT, the outer magnetosphere at  $L > 5$  was eliminated. The  
563 subsolar bow shock was located inside geosynchronous orbit at distances  $< 6.6$  Re that corresponded  
564 to the magnetopause standoff distance  $< 5$  Re.

565 5. The ring current dynamics under the extreme compression can be qualitatively described by the  
566 earthward transport with adiabatic betatron acceleration accompanied by violation of the third  
567 adiabatic invariant that resulted in accumulation of the particles in the inner magnetosphere at  $L < 4$ .

568 The lifetime of accelerated protons in the inner magnetosphere is obtained to be >10 times longer  
569 than typical one that explains “non-decaying” ring current observed after 19 UT.

570 6. We speculate that the anomalous dynamics of extremely compressed magnetosphere can be well  
571 described by the models if we accept the He abundance of ~30%, which is only slightly higher than  
572 the upper 27% threshold for He/H ratio obtained from Cluster measurements that is not unusual for  
573 erupting filaments. High helium abundances of >20% allow successful predicting the observations by  
574 the empirical models within the model errors.

575

576

## Appendix A

### 577 **On contribution of the ring current adiabatic compression to the negative $Dst^*$ variation**

578 During almost 2 hours from 1845 to 2055 UT, we observed an abrupt and very strong increase  
579 preceding a gradual and slow decrease of the solar wind dynamic pressure (see Figure 1). Such kind  
580 of pressure variation resonates with the drift periods of ring current (RC) particles (~ 2 hours). This  
581 giant pressure pulse resulted in irreversible shift of RC to the Earth. The particles of RC were  
582 accelerated in a betatron mechanism with keeping the first two adiabatic invariants of the drift motion  
583 that caused an intensification of RC and negative variation in  $Dst^*$ . The giant pressure pulse should  
584 affect the ring current in the same way as a sudden impulse affects the radiation belt during a storm  
585 sudden commencement. From this, we can estimate the magnetic effect produced by the RC  
586 intensification.

587 We will base the calculations on the values measured at  $t_1 \sim 1845$  UT on 21 January 2005, i.e. right  
588 before the beginning of extreme compression that can be attributed to the end of main phase and  
589 beginning of recovery phase of a magnetic storm, and at  $t_2 \sim 21.20$  UT 21 January 2005, i.e.  
590 immediately after the extreme compression and in the beginning of recovery phase of the following  
591 storm. Thereby, these two moments can be attributed to recovery phases of overlapping magnetic

592 storms. This approach greatly simplifies all calculations without specifying the unit system and  
 593 constant numerical factors, including the coefficients of the integrals. These coefficients are simply  
 594 reduced in the ratios presented below. Hereafter, unprimed quantities will refer to the time moment  $t_1$ ,  
 595 and primed – to the time moment  $t_2$ .

596 We will compare the deviations of relations calculated for the magnetic effect of RC, which is closed  
 597 in a trap and gradually compressed, with the following ratios:

$$598 \quad \frac{D_{st}'}{D_{st}} \approx \frac{80 \pm 10}{40 \pm 5} \approx 2.0 \pm 0.5, \quad (\text{A1})$$

$$599 \quad \frac{D_{st}^*'}{D_{st}^*} \approx \frac{115 \pm 15}{60 \pm 5} \approx 1.9 \pm 0.4, \quad (\text{A2a})$$

$$600 \quad \frac{D_{st}^{*'}}{D_{st}^*} \approx \frac{135 \pm 15}{60 \pm 5} \approx 2.3 \pm 0.4. \quad (\text{A2b})$$

601 The latter two ratios are written for the  $Dst$  variation corrected, respectively, on the pressure without  
 602 He contribution (see Figure 1) and on the “synthetic” pressure with strong He abundance (see Figure  
 603 9), which also contributes to the magnetosheath population.

604 We believe that at moments  $t_1$  and  $t_2$ , the contribution of the tail current was negligibly small (see  
 605 Figure 9) and RC was quasistationary. Hence, we can apply the Dessler-Parker-Sckopke theorem and  
 606 get:

$$607 \quad \frac{D_{st}^{*'}}{D_{st}^*} = \frac{W'}{W}, \quad (\text{A3})$$

608 where  $W$  – total kinetic energy of all particles in RC. Taking into account all methodic uncertainties,  
 609 we can consider only ion contribution to  $Dst$  and neglect a contribution of electrons. From statistical  
 610 consideration by *Kovtyukh* [2010], we can estimate that on average during the recovery phase, the



611 maximum of RC is located at  $L_m \approx 4.4 \pm 0.3$  under  $D_{st} \approx - (40 \pm 5)$  nT, i.e. before the extreme  
612 compression, and at  $L_m \approx 3.1 \pm 0.2$  under  $D_{st} \approx - (80 \pm 10)$  nT, i.e. after the extreme compression.  
613 During the interval between  $t_1$  and  $t_2$ , the noon magnetopause was located very deep inside  
614 geosynchronous orbit. However at the moments  $t_1$  and  $t_2$ , the magnetopause was quite close to  
615 geosynchronous orbit. Since the outer edge of RC is steep enough, we suppose for definition that at  
616 the beginning and end of the interval, the outer boundary was located at  $L_b \approx 6.6$ . With a more  
617 realistic position of the boundary and its offset in  $L$  during this period, our simplification has an  
618 uncertainty within 10%. That is considerably less than errors related to the uncertainty in localization  
619 of the RC maximum. Since the inner edge of RC is always much steeper than the outer one, we can  
620 neglect the contribution of particles in the inner edge to the RC total energy.  
621 The radial profile of pressure (energy density) of the hot magnetospheric plasma from the RC  
622 maximum to the outer edge of geomagnetic trap can be well approximated by the following  
623 expression:  $p(L) \approx a L^{-2} \exp(-L/L_0)$ , where  $L_0 \approx 2$  during recovery phase of magnetic storms  
624 [Kovtyukh, 2010]. The normalization parameter  $a$  varies from storm to storm. The ratio of the  
625 parameter values during the two time moments is equal to a ratio of RC pressures at those moment at  
626 the same  $L$ -shell, for instance at  $L = 5$ . As a rule, in the end of main phase and in the beginning of  
627 recovery phase, the ring current is quickly (within  $\sim 1$  hour) symmetrized by MLT. Therefore, we can  
628 expect that at the moments  $t_1$  and  $t_2$ , the ring current was almost symmetrical. Hence, in our  
629 calculations we suppose a symmetrical RC with isotropic pitch-angle distribution for simplicity.  
630 In the event considered, we can write the following equation for the dipole trap:

$$631 \quad \frac{W'}{W} = \frac{p'(L=5)}{p(L=5)} \times \frac{\int_{3.1 \pm 0.2}^{6.6} p'(L) L^2 dL}{\int_{4.4 \pm 0.3}^{6.6} p(L) L^2 dL} \quad (A4)$$

632 or

633 
$$\frac{W'}{W} = \frac{p'(L=5)}{p(L=5)} \times \frac{\int_{4.4 \pm 0.3}^{6.6} \exp(-L/L_0) dL}{\int_{4.4 \pm 0.3}^{6.6} \exp(-L/L_0) dL} \approx \frac{p'(L=5)}{p(L=5)} \times (2.5 \pm 0.8). \quad (\text{A5})$$

634 In order to adjust (A5) to (A2), we have to suppose

635 
$$\frac{p'(L=5)}{p(L=5)} \approx 0.76 - 0.92. \quad (\text{A6})$$

636 That is consistent both with the idea of RC compression and earthward displacement during the given  
 637 time interval and with the RC pressure values at  $L = 5$ , which have been obtained for other storms of  
 638 similar strength [see Table 2 in *Kovtyukh, 2010*].

639 Further, we calculate a relative change of the total number of RC ions ( $N$ ), which satisfies the inner  
 640 and outer boundaries of RC accepted here and relative increase of the RC pressure. To do this, we  
 641 have to select the shape of energy spectra of ions or the shape of the energy dependence for the ion  
 642 energy density (pressure). In according to experimental data [e.g., *Fritz et al., 1974*] the latter  
 643 relationship can be approximated by a Maxwellian distribution, such that the energy density ( $p$ ) and  
 644 the concentration of hot plasma ( $n$ ) are connected by a well-known simple relation:

645 
$$p(L) \propto E_m(L) n(L),$$

646 where  $E_m(L)$  is the location of maximum in the differential Maxwellian distribution. For simplicity,

647 we suppose that the value of  $E_m$  changes with  $L$  adiabatically, i.e.  $E_m \propto L^{-3}$ ,

648 and  $E_m' = E_m$  at  $L = 5$ . Then

649 
$$\frac{N'}{N} = \frac{p'(L=5)}{p(L=5)} \times \frac{\int_{4.4 \pm 0.3}^{6.6} L^3 \exp(-L/L_0) dL}{\int_{4.4 \pm 0.3}^{6.6} L^3 \exp(-L/L_0) dL} \quad (\text{A7})$$

650 or, after calculation of the integrals, we get:

651 
$$\frac{N'}{N} = \frac{p'(L=5)}{p(L=5)} \times (1.37 \pm 0.1). \quad (\text{A8})$$

652 Assuming that the ratio of pressures is the same as that in (A6), we can derive from (A8):

653 
$$\frac{N'}{N} = 1.16 \pm 0.19. \quad (\text{A9})$$

654 It means that during the extreme compression, a small amount of particles could be injected in the  
655 ring current.

656 In our calculations, the energy spectrum of RC ions could be approximated by more realistic  
657 function. However, it greatly complicated the calculations and made a little difference in the results.  
658 Under adiabatic compression of particles in quasi-dipole trap, the anisotropy of particle fluxes  
659 increases if mechanisms of fast isotropisation are absent. In addition, azimuthal asymmetry of RC  
660 could be changing during the period considered and could be different in the beginning and in the  
661 end. The difference could result in some changing in estimations (A6) and (A9) but could not change,  
662 apparently, the basic qualitative conclusions.

663 Thus, our calculations show that under simple assumptions, the change of  $Dst$  and  $Dst^*$ , observed  
664 from the moment right before the extreme magnetosphere compression to the moment immediately  
665 after the compression on 21 January 2005 (relations (A1) and (A2)), can be explained by a  
666 compression of the magnetic trap and adiabatical acceleration of RC particles.

667

668 **Acknowledgments.** The authors thank NASA/GSFC ISTP for providing data from the ACE, GOES,  
669 LANL and Cluster satellites. We are grateful to Cluster CIS and FGM instrument teams who have  
670 created the CIS (CODIF and HIA) and FGM instruments, and made their data available to the  
671 community. In particular, we greatly appreciate the anonymous Reviewer for providing the Cluster  
672 plasma data from the more recent calibrations of the CIS team. We thank C. W. Smith from the  
673 University of New Hampshire for providing the ACE magnetic data, and R. Skoug from Los Alamos  
674 National Laboratory for providing the ACE plasma data. We also thank NASA and NOAA for

675 providing the GOES magnetic data, Los Alamos National Laboratory for providing the LANL  
676 plasma data, and Kyoto World Data Center for Geomagnetism for providing the Dst and ASY/SYM  
677 indices. Simulation results of SWMF/BATS-R-US code have been provided by the Community  
678 Coordinated Modeling Center at Goddard Space Flight Center through their public Runs on Request  
679 system (<http://ccmc.gsfc.nasa.gov>). The CCMC is a multi-agency partnership between NASA,  
680 AFMC, AFOSR, AFRL, AFWA, NOAA, NSF and ONR. This work was supported by grants  
681 NSC102-2111-M-008-023 from the National Science Council of Taiwan and by Ministry of  
682 Education under the Aim for Top University program 102G901-27 at National Central University of  
683 Taiwan as well as by RFBR grant 13-02-00461 and Programs P22, P26 of the RAS Presidium at  
684 MSU SINP and IKI.

685

## 686 **References**

- 687 Bailey, J., and M. Gruntman (2013), Observations of exosphere variations during geomagnetic  
688 storms, *Geophys. Res. Lett.*, *40*, 1907-1911, doi:10.1002/grl.50443.
- 689 Baker, D. N., et al. (2013), A major solar eruptive event in July 2012: Defining extreme space  
690 weather scenarios, *Space Weather*, doi:10.1002/swe.20097.
- 691 Balogh, A., et al. (2001), The Cluster Magnetic Field Investigation: Overview of in-flight  
692 performance and initial results, *Ann. Geophys.*, *19*, 1207-1217.
- 693 Belov, A. V., et al. (2005), Ground level enhancement of the solar cosmic rays on January 20, 2005,  
694 *Proc. 29th Internat. Cosmic Ray Conf. (Pune)*, *1*, 189-192.
- 695 Borovsky, J. E., M. F. Thomsen, and R. C. Elphic (1998), The driving of the plasma sheet by the  
696 solar wind, *J. Geophys. Res.*, *103*, 17,617–17,639, doi:10.1029/97JA02986.
- 697 Borrini, G., et al. (1982), Helium abundance enhancements in the solar wind, *J. Geophys. Res.*,  
698 *87(A9)*, 7370-7378, doi:10.1029/JA087iA09p07370.
- 699 Burlaga, L., et al. (1998), A magnetic cloud containing prominence material: January 1997, *J.*  
700 *Geophys. Res.*, *103(A1)*, 277-285, doi:0.1029/97JA02768.

701 Burton R. K., R. L. McPherron, and C. T. Russell (1975), An empirical relationship between  
702 interplanetary conditions and Dst, *J. Geophys. Res.*, 80, 4204-4214,  
703 doi:10.1029/JA080i031p04204.

704 Cairns, I. H., et al. (1995), Unusual locations of Earth's bow shock on September 24-25, 1987: Mach  
705 number effects, *J. Geophys. Res.*, 100(A1), 47-62, doi:10.1029/94JA01978.

706 Chao, J.-K., et al. (2002), Models for the size and shape of the Earth's magnetopause and bow shock,  
707 in *Space Weather Study Using Multipoint Techniques*, Ed. L.-H. Lyu, 360 pp., Pergamon, New  
708 York, 127 – 135.

709 Chapman, S., and V. C. A. Ferraro (1931), A new theory of magnetic storms, *J. Geophys. Res.*, 36,  
710 77-97. *Nature*. 1930, 126, 129–130.

711 Claflin, E. S. (1970), Charge exchange cross section for hydrogen and helium ions incident on atomic  
712 hydrogen: 1 to 1000 keV, *Rep. TR-0059 (6260-20)-1. Aerosp. Corp.*, El Segundo, Calif., July  
713 1970.

714 Cornwall, J. M., and M. Schulz (1979), Physics of heavy ions in the magnetosphere, *Solar System*  
715 *Plasma Physics*, Eds. E. N. Parker, C. F. Kennel, and L. J. Lanzerotti, North-Holland,  
716 Amsterdam, 3, 165-210.

717 Crooker, N. U., et al. (2000), Density extremes in the solar wind, *Geophys. Res. Lett.*, 27(23), 3769–  
718 3772.

719 Chen, P. F. (2011), Coronal mass ejections: Models and their observational basis, *Living Rev. Solar*  
720 *Phys.*, 8, 1–92.

721 Dandouras, I. S., et al. (2009), Magnetosphere response to the 2005 and 2006 extreme solar events as  
722 observed by the Cluster and Double Star spacecraft, *Adv. Space Res.*, 43, 618-623,  
723 doi:10.1016/j.asr.2008.10.015.

724 DeForest, S. E. (1973), Detection of the solar wind at synchronous orbit, *J. Geophys. Res.*, 78, 1195-  
725 1197.

726 Dmitriev, A., and A. Suvorova (2012), Equatorial trench at the magnetopause under saturation, *J.*  
727 *Geophys. Res.*, *117*, A08226, doi:10.1029/2012JA017834.

728 Dmitriev, A. V., J.-K. Chao, and D.-J. Wu (2003), Comparative study of bow shock models using  
729 Wind and Geotail observations, *J. Geophys. Res.*, *108*(A12), 1464, doi:10.1029/2003JA010027.

730 Dmitriev, A. V., et al. (2005a), Geosynchronous magnetopause crossings on 29-31 October 2003, *J.*  
731 *Geophys. Res.*, *110*, A08209, doi:10.1029/2004JA010582.

732 Dmitriev, A. V., et al. (2005b), Indirect estimation of the solar wind conditions in 29–31 October  
733 2003, *J. Geophys. Res.*, *110*, A09S02, doi:10.1029/2004JA010806.

734 Dmitriev, A., A. Suvorova, and J.-K. Chao (2011), A predictive model of geosynchronous  
735 magnetopause crossings, *J. Geophys. Res.*, *116*, A05208, doi:10.1029/2010JA016208.

736 Du, A. M., B. T. Tsurutani, and W. Sun (2008), Anomalous geomagnetic storm of 21–22 January  
737 2005: A storm main phase during northward IMFs, *J. Geophys. Res.*, *113*, A10214,  
738 doi:10.1029/2008JA013284.

739 Fairfield, D. H. (1971), Average and unusual locations of the Earth's magnetopause and bow shock, *J.*  
740 *Geophys. Res.*, *76*(28), 6700-6716, doi:10.1029/JA076i028p06700.

741 Feldstein, Ya. I., V. I. Pisarsky, N. M. Rudneva, and A. Grafe (1984) Ring current simulation in  
742 connection with interplanetary space conditions, *Planet. Space Sci.*, *32*, 975–984.

743 Fenrich, F. R., and J. G. Luhmann (1998), Geomagnetic response to magnetic clouds of different  
744 polarity, *Geophys. Res. Lett.*, *25*, 2999-3002.

745 Formisano, V. (1973), On the March 7-8, 1970 event, *J. Geophys. Res.*, *73*, 1198-1202.

746 Formisano, V. (1979), Orientation and shape of the Earth's bow shock in three dimensions, *Planet.*  
747 *Space Sci.*, *27*, 1151-1161.

748 Foullon, C., et al. (2007), Multi-Spacecraft Study of the 21 January 2005 ICME Evidence of Current  
749 Sheet Substructure Near the Periphery of a Strongly Expanding, Fast Magnetic Cloud, *Solar*  
750 *Phys.*, *244*, 139-165, doi:10.1007/s11207-007-0355-y.

751 Fritz, T. A., et al. (1974), Initial observations of magnetospheric boundaries by Explorer 45 ( $S^3$ ),  
752 *Correlated Interplanetary and Magnetospheric Observations*, Ed. D. E. Page, Dordrecht–  
753 Holland: D. Reidel, pp. 485–506.

754 Ganushkina, N. Yu., M. W. Liemohn, M. V. Kubyshkina, R. Ilie, and H. J. Singer (2010), Distortions  
755 of the magnetic field by storm-time current systems in Earth's magnetosphere, *Ann. Geophys.*, 28,  
756 123-140, doi:10.5194/angeo-28-123-2010.

757 Gopalswamy, N., et al. (2005), Introduction to violent Sun-Earth connection events of October -  
758 November 2003, *J. Geophys. Res.*, 110, A09S00, doi:10.1029/2005JA011268.

759 Gosling, J. T., et al. (1980) Observations of large fluxes of  $He^+$  in the solar wind following an  
760 interplanetary shock, *J. Geophys. Res.*, 85(A7), 3431-3434, doi: 10.1029/JA085iA07p03431.

761 Gosling, J. T., et al. (1982), Evidence for quasi-stationary reconnection at the dayside magnetopause,  
762 *J. Geophys. Res.*, 87(A4), 2147-2158, doi:10.1029/JA087iA04p02147.

763 Hoffman R. A., L. J. Cahill, Jr., R. R. Anderson, et al. (1975), Explorer 45( $S^3$ -A) observations of the  
764 magnetosphere and magnetopause during August 4-6, 1972, magnetic storm period, *J. Geophys.*  
765 *Res.*, 80(31), 4287-4296.

766 Hudson, M. K., et al. (1997), Simulations of radiation belt formation during storm sudden  
767 commencements, *J. Geophys. Res.*, 102(A7), 14087-14102, doi:10.1029/97JA03995.

768 Hudson, M. K., et al. (2004), 3D modeling of shock-induced trapping of solar energetic particles in  
769 the Earth's magnetosphere, *J. Atmosph. Solar-Terr. Phys.*, 66, 1389-1397,  
770 doi:10.1016/j.jastp.2004.03.024.

771 Kistler, L. M., et al. (1989), Energy spectra of the major ion species in the ring current during  
772 geomagnetic storms, *J. Geophys. Res.*, 94(A4), 3579–3599.

773 Kovtyukh, A. S. (2001), Geocorona of hot plasma, *Cosmic Res.*, 39(6), 527-558.

774 Kovtyukh, A. S. (2010), Radial profile of pressure in a storm ring current as a function of  $D_{st}$ , *Cosmic*  
775 *Res.*, 48(3), 211–231.

776 Kuznetsov, S. N., and A. V. Suvorova (1998), An empirical model of the magnetopause for broad  
777 ranges of solar wind pressure and Bz IMF, in *Polar Cap Boundary Phenomena*, NATO ASI Ser.,  
778 Eds. J. Moen, A. Egeland, and M. Lockwood, pp. 51-61, Kluwer Acad., Norwell, Mass.

779 Kuznetsov, S. N., et al. (2005), Proton acceleration during 20 January 2005 solar flare: CORONAS-F  
780 observations of high-energy gamma emission and GLE, *29th International Cosmic Ray*  
781 *Conference, Pune, 1*, 49-52.

782 Kuznetsova, T. V., and A. I. Laptukhov (2011), Contribution of geometry of interaction between  
783 interplanetary and terrestrial magnetic fields into global magnetospheric state and geomagnetic  
784 activity, *Adv. Space Res.*, *47*, 978-990.

785 Lazutin, L. L., and S. N. Kuznetsov (2008), Nature of sudden auroral activations at the beginning of  
786 magnetic storms, *Geomag. and Aeron.*, *48(2)*, 165–174.

787 Lazutin, L. L., et al. (2010), Dynamics of solar protons in the Earth's magnetosphere during magnetic  
788 storms in November 2004 – January 2005, *Geomag. and Aeron.*, *50(2)*, 176-188.

789 Lockwood, J. A., L. Hsieh, and J. J. Quenby (1975), Some unusual features of the cosmic ray storm  
790 in August 1972, *J. Geophys. Res.*, *80*, 1725-1734, doi:10.1029/JA080i013p01725.

791 Lu, G., et al. (1998), Global energy deposition during the January 1997 magnetic cloud event, *J*  
792 *Geophys. Res.*, *103(A6)*, 11,685-11,694, doi:10.1029/98JA00897.

793 McPherron, R. L., and T. P. O'Brien (2001), Predicting geomagnetic activity: The Dst index, in *Space*  
794 *Weather, Geophys. Monogr. Ser., vol. 125*, edited by P. Song, H. J. Singer, and G. L. Siscoe, 339-  
795 345, AGU, Washington, D. C.

796 McKenna-Lawlor, S., et al. (2010), Moderate geomagnetic storm (21-22 January 2005) triggered by  
797 an outstanding coronal mass ejection viewed via energetic neutral atoms, *J. Geophys. Res.*, *115*,  
798 A08213, doi:10.1029/2009JA014663.

799 Ober, D. M., M. F. Thomsen, and N. C. Maynard (2002), Observations of bow shock and  
800 magnetopause crossings from geosynchronous orbit on 31 March 2001, *J. Geophys. Res.*,  
801 *107(A8)*, 1206, doi:10.1029/2001JA000284.



802 O'Brien, T. P., and R. L. McPherron (2000), An empirical phase space analysis of ring current  
803 dynamics: Solar wind control of injection and decay, *J. Geophys. Res.*, *105*, 7707- 7719.

804 O'Brien, T. P., and R. L. McPherron (2002), Seasonal and diurnal variation of Dst dynamics, *J.*  
805 *Geophys. Res.*, *107*(A11), 1341, doi:10.1029/2002JA009435.

806 Østgaard, N. (2003), Neutral hydrogen density profiles derived from geocoronal imaging, *J.*  
807 *Geophys. Res.*, *108*(A7), 1300, doi:10.1029/2002JA009749.

808 Peredo, M., et al. (1995), Three-dimensional position and shape of the bow shock and their variations  
809 with Alfvénic, sonic, and magnetosonic Mach numbers and interplanetary magnetic field  
810 orientation, *J. Geophys. Res.*, *100*, 7907-7916, doi:10.1029/94JA02545.

811 Pudovkin, M. I., S. A. Zaitseva, and I. Z. Sizova (1985), Growth rate and decay of magnetospheric  
812 ring current, *Planet. Space Sci.*, *33*(10), 1097-1102.

813 Rème, H., et al. (2001), First multispacecraft ion measurements in and near the Earth's  
814 magnetosphere with the identical Cluster Ion Spectrometry (CIS) experiment, *Ann. Geophys.*, *19*,  
815 1303-1354.

816 Richard, R. L., et al. (2009), Modeling the entry and trapping of solar energetic particles in the  
817 magnetosphere during the November 24-25, 2001 storm, *J. Geophys. Res.*, *114*, A04210,  
818 doi:10.1029/2007JA012823.

819 Russell, C. T., and S. M. Petrinec (1996), Comment on "Towards an MHD theory for the standoff  
820 distance of Earth's bow shock" by I. H. Cairns and C. L. Grabbe, *Geophys. Res. Lett.*, *23*, 309-  
821 310, doi:10.1029/95GL03505.

822 Russell, C. T., et al. (2000), The extreme compression of the magnetosphere, May 4, 1998, as  
823 observed by the POLAR spacecraft, *Adv. Space Res.*, *25*, 1369-1375. doi:10.1016/S0273-  
824 1177(99)00646-8.

825 Russell, C. T., et al. (2013), The very unusual interplanetary coronal mass ejection of 2012 July 23: A  
826 blast wave mediated by solar energetic particles, *Astrophys. Jour.*, *770*, 38.

827 Schwenn R. (1983), Direct correlations between coronal transients and interplanetary disturbances,  
828 *Space Science Reviews*, 34(1), 85-99.

829 Sharma, R., et al. (2013), Interplanetary and geomagnetic consequences of 5 January 2005 CMEs  
830 associated with eruptive filaments, *J. Geophys. Res.*, 118, 3954-3967, doi:10.1002/jgra.50362.

831 Song, P., et al. (2001), Polar observations and model predictions during May 4, 1998, magnetopause,  
832 magnetosheath, and bow shock crossings, *J. Geophys. Res.*, 106, 18,927-18,942,  
833 doi:10.1029/2000JA900126.

834 Spreiter, J. R., A. L. Summers, and A. Y. Alksne (1966), Hydromagnetic flow around the  
835 magnetosphere, *Planet. Space Sci.*, 14, 223-253.

836 Suvorova A. V, A. V. Dmitriev, S. N. Kuznetsov (1999), Dayside magnetopause models, *Rad. Meas.*,  
837 30(5), 687-692.

838 Suvorova A., et al. (2005), Necessary conditions for the geosynchronous magnetopause crossings, *J.*  
839 *Geophys. Res.*, 110, A01206, doi:10.1029/2003JA010079.

840 Troshichev, O., D. Sormakov, A. Janzhura (2011a), Relation of PC index to the geomagnetic storm  
841 Dst variation, *J. Atmosph. Solar-Terr. Phys.*, 73, 611-622.

842 Troshichev, O. A., N. A. Podorozhkina, A. S. Janzhura (2011b), Relationship between PC index and  
843 magnetospheric substorms observed under conditions of northward IMF, *J. Atmosph. Solar-Terr.*  
844 *Phys.*, 73, 2373-2378.

845 Tsurutani, B. T., et al. (2003), The extreme magnetic storm of 1-2 September 1859, *J. Geophys. Res.*,  
846 108(A7), 1268, doi:10/1029/2002JA009504.

847 Tsyganenko, N. A. (2000), Solar wind control of the tail lobe magnetic field as deduced from Geotail,  
848 AMPTE/IRM, and ISEE 2 data, *J. Geophys. Res.*, 105, 5517-5528, doi:10.1029/1999JA000375.

849 Tsyganenko, N. A., and M. I. Sitnov (2005), Modeling the dynamics of the inner magnetosphere  
850 during strong geomagnetic storms, *J. Geophys. Res.*, 110, A03208, doi:10.1029/2004JA010798.

851 Vaisberg, O., and G. Zastenker (1976), Solar wind and magnetosheath observations at earth during  
852 August 1972, *Space Science Reviews*, 19, 687-702.

853 Verigin, M. I., et al. (2001), Analysis of the 3-D shape of the terrestrial bow shock by  
854 Interball/MAGION 4 observations, *Adv. Space Res.*, 28, 857-862.

855 Wang, C. B., J.-K. Chao, and C. H. Lin (2003), Influence of the solar wind dynamic pressure on the  
856 decay and injection of the ring current, *J. Geophys. Res.*, 108(A9), 1341,  
857 doi:10.1029/2003JA009851.

858

859 **Table 1.** Observations of the bow shock ( $R_{BS}$ ) and magnetopause ( $R_{MP}$ ) inside geosynchronous orbit

Date time	Satellites	$R_{BS}$ , Re (zenith angle) duration	$R_{MP}$ , Re (zenith angle)	$V$ , km/s	$D$ cm <sup>-3</sup>	$Pd$ nPa	IMF B Bz nT	Ph*	Reference
1970 8 Mar ~20 UT	ATS-5 HEOS-1	$\leq 6.6(0^\circ)$ 3 min	$< 6.6(0^\circ)$	880	$\sim 40$	$> 50$	$\sim 30$ $> 0$	0	<i>DeForest, 1973</i> <i>Formisano, 1973</i>
1972 4 Aug ~23 UT	Explorer-45 Prognoz-2 HEOS-2	$\sim 10(75^\circ)$ -	$5.2(45^\circ)$ $6(40^\circ)$	1700	$\sim 30$	$\geq 150$	$> 50$ $\pm$	2	<i>Hoffman et al., 1975</i> <i>Lockwood et al., 1975</i> <i>Vaisberg and Zastenker, 1976</i>
1998 4 May ~07 UT	Polar WIND ACE	$7.3(32^\circ)$ 2 min	$5.3(19^\circ)$	800	60	$> 65$	20 $> 0$	2	<i>Russell et al., 2000</i> <i>Song et al., 2001</i>
2001 31 Mar ~05 UT	1994-084 ACE IMP8	$\leq 6.6(0^\circ)$ 10 min	$< 6.6(90^\circ)$	700	$\sim 70$	$> 60$	$\sim 50$ $< 0$	0	<i>Ober et al., 2002</i>
2003 30 Oct 22UT	GOES-10 ACE	$\leq 6.6(15^\circ)$ 2 min	$< 6.6$	1200	-	$> 40$	20 $> 0$	2	<i>Dmitriev et al., 2005a,b</i> <i>Veselovsky et al., 2004</i>
2005 21 Jan ~19UT	GOES DBST-1 ACE Cluster	$\leq 6.6(0^\circ)$ 40 min 2 hours**	$< 6.6$	1000	$\sim 60$	$> 90$	40 $\pm$	1	<i>Foullon et al., 2007</i> <i>Du et al., 2008</i> <i>Dandouras et al., 2009</i> <i>McKenna-Lawlor et al., 2010</i>

860 \* Phase of the storm: 0 - onset, 1 - main, 2 - recovery

861 \*\* Shown at present study

862

863

864 **Table 2.** Predicted bow shock subsolar distances and dynamic pressure

Model	$R_s$ , Re	$Pd$ , nPa
<i>Formisano</i> [1979]	4.4	1500
<i>Cairns et al.</i> [1995]	4.5	-
<i>Peredo et al.</i> [1995]	5.3	1500
<i>Russell and Petrinec</i> [1996]	5.4	140
BSV [ <i>Verigin et al.</i> , 2001]	5.2	80
BSC [ <i>Chao et al.</i> , 2002]	8.	75

865  
866

867 **Figure Captions**

868

869 **Figure 1.** Heliospheric and geomagnetic conditions during magnetic storm on 21 January 2005 (from  
870 top to bottom): fluxes of solar energetic particles (SEP), solar wind velocity  $V$ , solar wind proton  
871 density  $D$ , helium contribution; solar wind dynamic pressure  $Pd$ , IMF  $B_x$ ,  $B_y$  and  $B_z$  components in  
872 GSM,  $AE$  and  $Dst$  geomagnetic indices. Solar wind plasma and IMF parameters measured by ACE  
873 and Cluster are shown, respectively, by red and blue curves. The time profiles of ACE and Cluster  
874 are shifted by the time of the solar wind propagation. Hourly  $Dst$  and 1-min SYM-H index are shown  
875 by gray histogram and black curves. At the bottom panel,  $Dst^*$  is corrected by pressure acquired from  
876 ACE (red curve) and Cluster (blue curve). See details in the text.

877

878 **Figure 2.** Prediction results for the 1-hour  $Dst$  variation during magnetic storm on 21 – 22 January  
879 2005 using different empirical models. The beginning of the storm from 17 to 19 UT is predicted  
880 quite well. The models fail after 19 UT, when the  $Dst$  index continues decreasing despite of  
881 northward IMF orientation.

882

883 **Figure 3.** Location in GSM of geosynchronous and high-apogee satellites at ~1850 UT on 21 January  
884 2005 in X-Y plane (left panel) and X-Z plane (right panel). In the X-Y plane, the position of bow  
885 shock (red curve) and magnetopause (blue curve) are calculated, respectively, by BSV [Verigin *et al.*,  
886 2001] and KS98 [Suvorova *et al.*, 1999] empirical models for the extreme solar wind conditions.  
887 Under such conditions, the subsolar bow shock and whole dayside magnetopause are located inside  
888 geosynchronous orbit.

889

890 **Figure 4.** Geosynchronous magnetopause (vertical blue dashed lines) and bow shock (vertical red  
891 dashed lines) crossings observed by GOES-10 (a) and GOES-12 (b) on 21 January 2005. The panels  
892 show (from top to bottom): solar wind dynamic pressure calculated from the ACE (red curve) and

893 Cluster (blue curve) data and modeled dynamic pressure  $P_{gmc}$  required for magnetopause  
894 geosynchronous crossing [Dmitriev *et al.*, 2011]; geocentric distance to the bow shock modeled by  
895 BSC model [Chao *et al.*, 2002] for the ACE (red curve) and Cluster (blue curve) pressure, and  
896 geocentric distance to the magnetopause (black curve) modeled by KS98 model [Suvorova *et al.*,  
897 1999] for the Cluster pressure;  $B_z$ ,  $B_y$  and  $B_x$  observed by the satellites GOES (black curves) and  
898 Cluster-3 (blue curves) and predicted by a global MHD model (red curves); magnetic local time of  
899 GOES. At panel (b), the bow shock distance was calculated for the Cluster pressure by the BSC  
900 model (red) and by a model BSV [Verigin *et al.*, 2001]. The magnetopause and bow shock were  
901 calculated for the corresponding GOES angular location. Note that GOES-10 and GOES-12 were  
902 situated in the interplanetary medium from 1845 to 2035 UT and from 1845 to 2010 UT,  
903 respectively.

904

905 **Figure 5.** Geosynchronous magnetopause crossing (vertical blue dashed line) observed by LANL-  
906 1997 on 21 January 2005. The panels show (from top to bottom): solar wind dynamic pressure  
907 calculated from Cluster (blue curve) data and modeled dynamic pressure  $P_{gmc}$ ; KS98 model  
908 prediction of the geocentric distance to the magnetopause (black curve) for the Cluster pressure;  
909 plasma ratios RI (red curve) and RE (blue curve, see details in the text); magnetic local time. LANL-  
910 1997 encountered with the magnetosheath at ~0530MLT.

911

912 **Figure 6.** Temporal dynamics of pitch-angle anisotropy for the protons with energies  $>30$  keV (black  
913 crosses) and  $>100$  keV (blue triangles) observed by POES-17 near the noon-midnight meridian at  $L \sim$   
914 5 on 21 January 2005. From ~19 to ~22 UT (restricted by red dashed lines), the anisotropy was less  
915 than or about 1 indicating that the majority of protons were not trapped at  $L \sim 5$ .

916

917 **Figure 7.** Dynamics of proton integral spectra observed by POES-17 satellite near the noon-midnight  
918 meridian on 21 – 22 January 2005: (a) at  $L = 2$ ; (b) at  $L = 3$ ; (c) at  $L = 4$ ; (d) at  $L = 5$ . Different

919 symbols and colors correspond to different observation times: blue diamonds – 17 UT, red triangles –  
920 21 UT on 21 January and green diamonds – 05 UT on 22 January. At 21 UT, the fluxes of low-  
921 energy protons ( $<1$  MeV) increased in the inner magnetosphere ( $L < 4$ ) by more than 10 times.

922

923 **Figure 8.** Temporal variations of 1 – 5 MeV protons observed by CORONAS-F satellite on 21 – 22  
924 January, 2005. Black curve with squares corresponds to a region of  $L = 1 - 2$ , red curve with triangles  
925 –  $L = 2 - 3$ , blue curve with diamonds –  $L = 3 - 4$ , and pink curve with crosses –  $L = 4 - 5$ . After  
926 18UT on 21 January, the proton fluxes increased substantially in the inner magnetosphere.

927

928 **Figure 9.** Observed and proposed variations of the solar wind plasma and geomagnetic parameters on  
929 21 January 2005 (from top to bottom): helium contribution He/H measured by Cluster C4 (blue  
930 curve) and 4-time magnified one (red curve); solar wind dynamic pressure  $P_d$  calculated from Cluster  
931 C-4 data (blue curve) and with using the magnified He/H (red curve); nose distances to the bow  
932 shock and magnetopause predicted by the models BSC(red curve), BSV (blue curve) and KS98  
933 (black curve) for the magnified He/H;  $Dst$  variation observed (black curve) and normalized by the  
934 observed  $P_d$  (blue curve) and by the magnified  $P_d$  (red curve) as well as a driving parameter  $\varepsilon$  for the  
935 tail current (dotted green curve, right axis). The vertical red dashed lines restrict the interplanetary  
936 interval when the subsolar magnetopause was located upstream of the bow shock. The assumption of  
937 strong helium contribution of  $\sim 30\%$  allows resolving the discrepancies between the observations and  
938 model predictions.

939

940 **Figure 10.** Variations of plasma parameters measured by Cluster on 21 January 2005 (from top to  
941 bottom): CODIF C4 energy-time spectrograms (in particle energy flux units) for  $H^+$  and  $He^{++}$ ; the  
942 corresponding densities of  $H^+$  and  $He^{++}$ ; Cluster C1 HIA (no mass discrimination) ion energy-time  
943 spectrogram and corresponding density. The data come from the more recent calibrations of the CIS  
944 team (acquired from private communication with anonymous Reviewer of this paper).



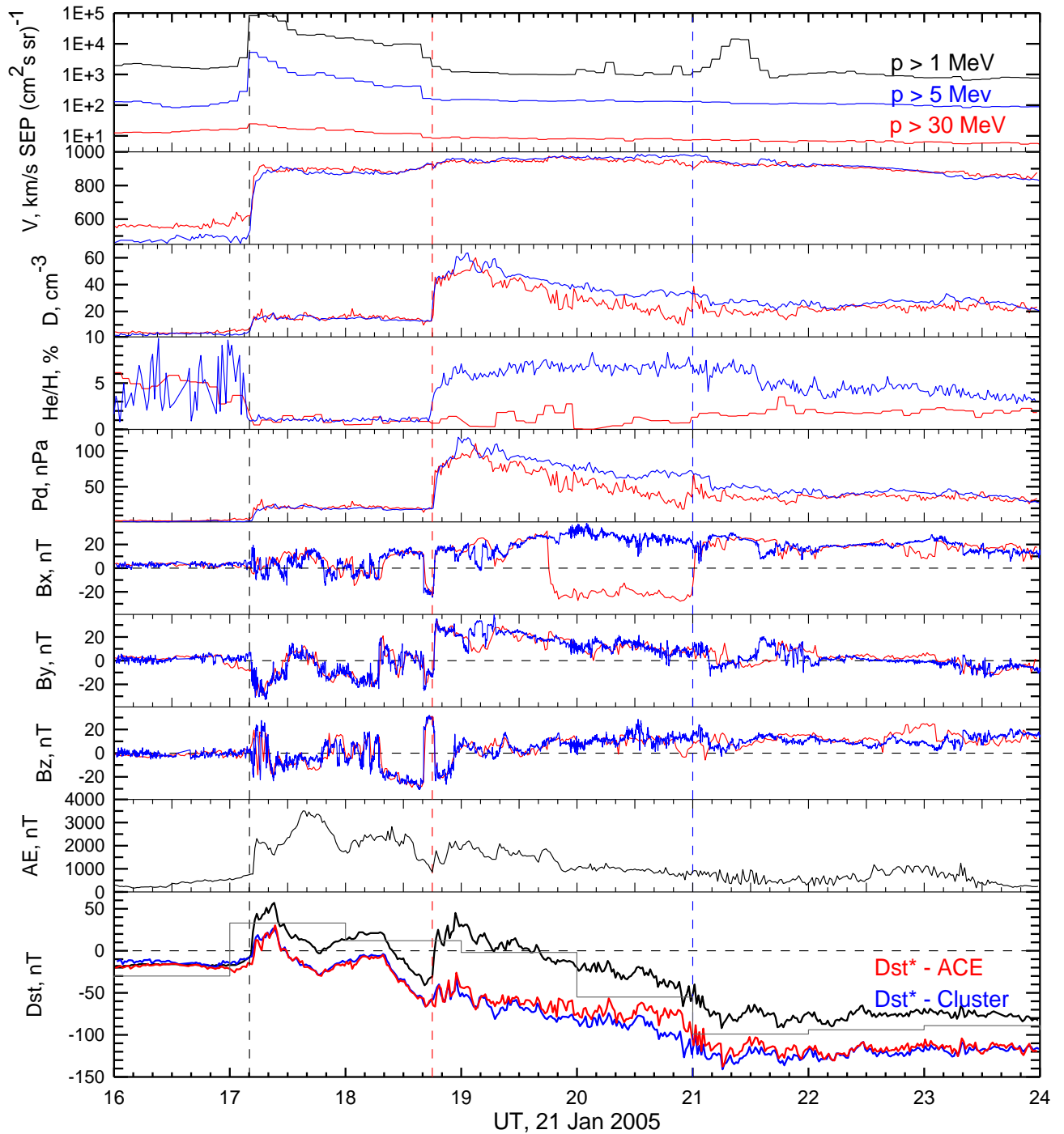


Figure 1. Heliospheric and geomagnetic conditions during magnetic storm on 21 January 2005 (from top to bottom): fluxes of solar energetic particles (SEP), solar wind velocity  $V$ , solar wind proton density  $D$ , helium contribution; solar wind dynamic pressure  $Pd$ , IMF  $B_x$ ,  $B_y$  and  $B_z$  components in GSM,  $AE$  and  $Dst$  geomagnetic indices. Solar wind plasma and IMF parameters measured by ACE and Cluster are shown, respectively, by red and blue curves. The time profiles of ACE and Cluster are shifted by the time of the solar wind propagation. Hourly  $Dst$  and 1-min SYM-H index are shown by gray histogram and black curves. At the bottom panel,  $Dst^*$  is corrected by pressure acquired from ACE (red curve) and Cluster (blue curve). See details in the text.

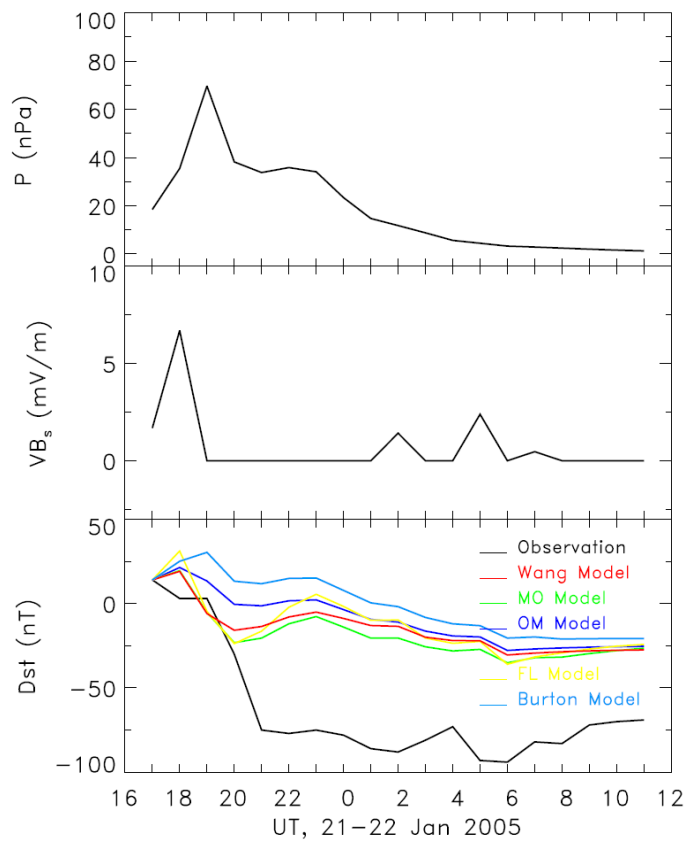


Figure 2. Prediction results for the 1-hour Dst variation during magnetic storm on 21 – 22 January 2005 using different empirical models. The beginning of the storm from 17 to 19 UT is predicted quite well. The models fail after 19 UT, when the Dst index continues decreasing despite of northward IMF orientation.

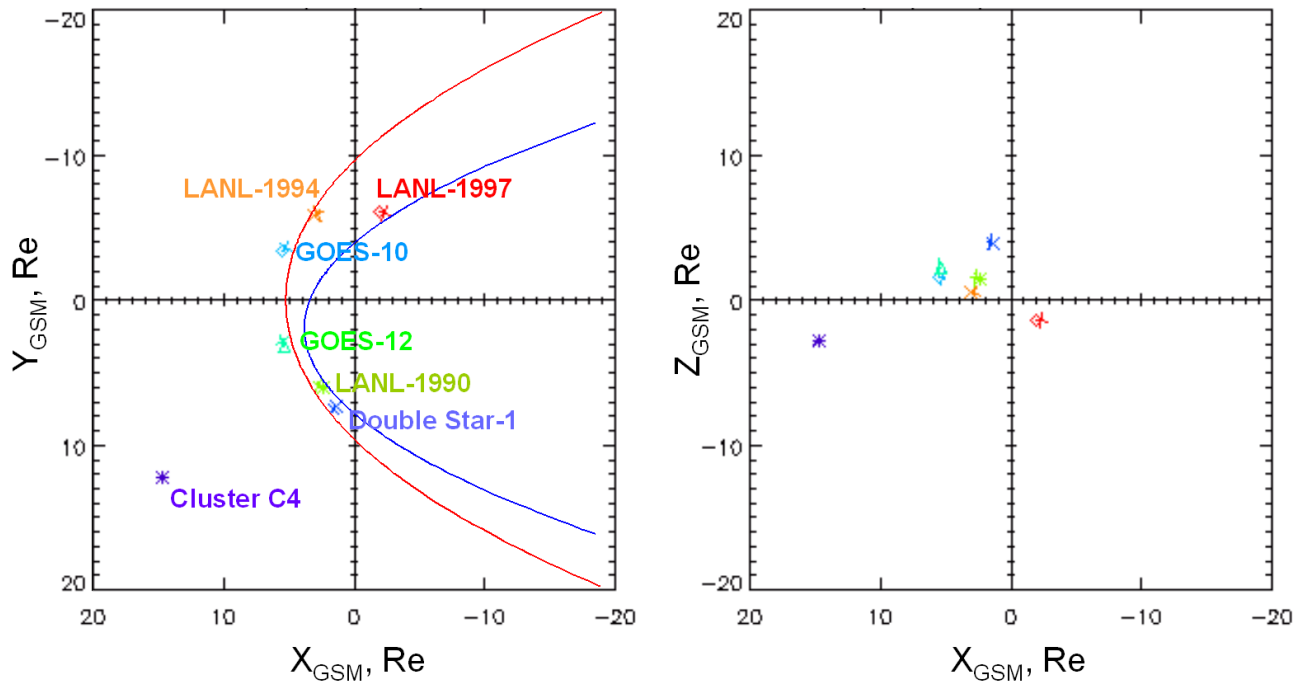
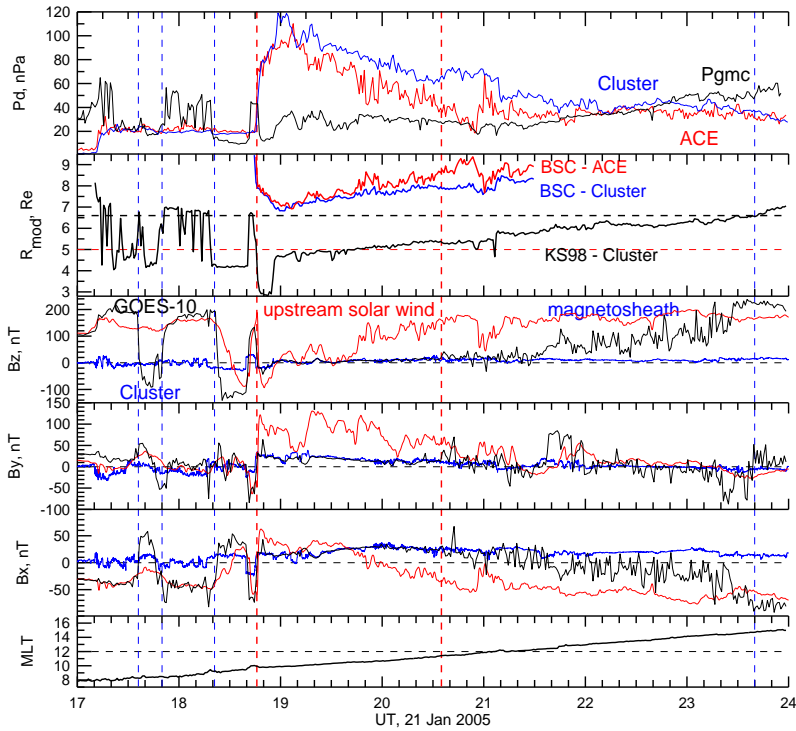
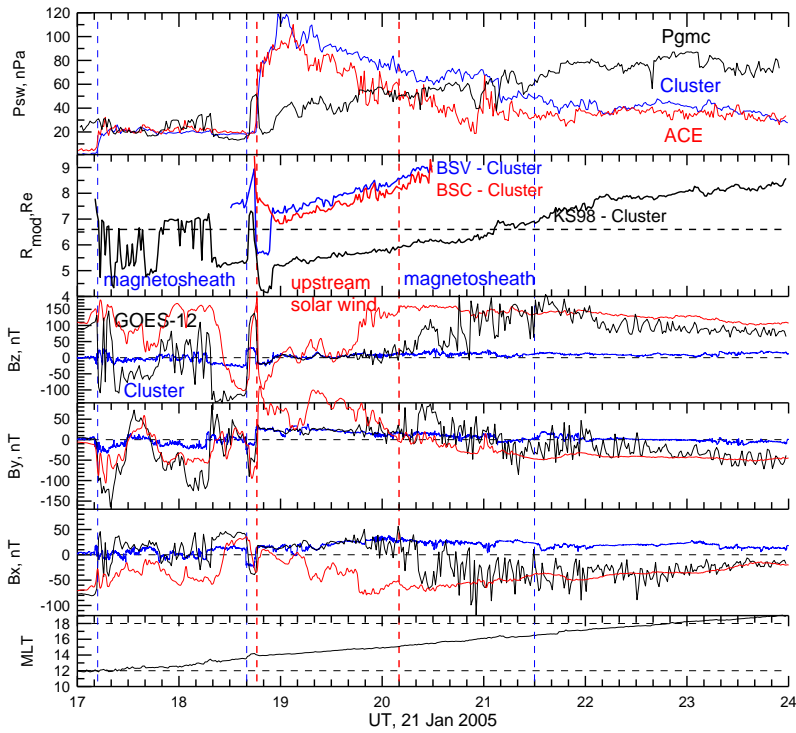


Figure 3. Location in GSM of geosynchronous and high-apogee satellites at ~1850 UT on 21 January 2005 in X-Y plane (left panel) and X-Z plane (right panel). In the X-Y plane, the position of bow shock (red curve) and magnetopause (blue curve) are calculated, respectively, by BSV [Verigin *et al.*, 2001] and KS98 [Suvorova *et al.*, 1999] empirical models for the extreme solar wind conditions. Under such conditions, the subsolar bow shock and whole dayside magnetopause are located inside geosynchronous orbit.



a



b

Figure 4. Geosynchronous magnetopause (vertical blue dashed lines) and bow shock (vertical red dashed lines) crossings observed by GOES-10 (a) and GOES-12 (b) on 21 January 2005. The panels show (from top to bottom): solar wind dynamic pressure calculated from the ACE (red curve) and Cluster (blue curve) data and modeled dynamic pressure  $P_{gmC}$  required for magnetopause geosynchronous crossing [Dmitriev *et al.*, 2011]; geocentric distance to the bow shock modeled by BSC model [Chao *et al.*, 2002] for the ACE (red curve) and Cluster (blue curve) pressure, and geocentric distance to the magnetopause (black curve) modeled by KS98 model [Suvorova *et al.*, 1999] for the Cluster pressure;  $B_z$ ,  $B_y$  and  $B_x$  observed by the satellites GOES (black curves) and Cluster-3 (blue curves) and predicted by a global MHD model (red curves); magnetic local time of GOES. At panel (b), the bow shock distance was calculated for the Cluster pressure by the BSC model (red) and by a model BSV [Verigin *et al.*, 2001]. The magnetopause and bow shock were calculated for the corresponding GOES angular location. Note that GOES-10 and GOES-12 were situated in the interplanetary medium from 1845 to 2035 UT and from 1845 to 2010 UT, respectively.

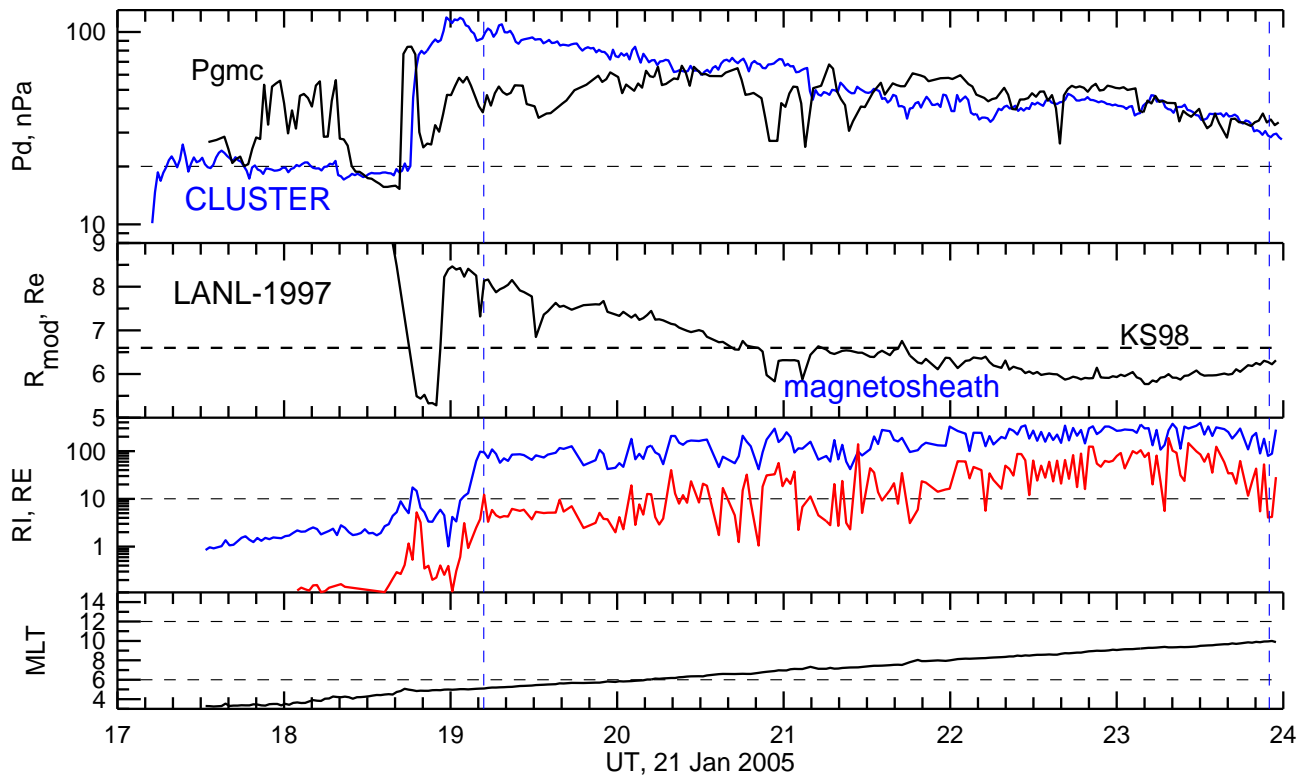


Figure 5. Geosynchronous magnetopause crossing (vertical blue dashed line) observed by LANL-1997 on 21 January 2005. The panels show (from top to bottom): solar wind dynamic pressure calculated from Cluster (blue curve) data and modeled dynamic pressure  $P_{gmc}$ ; KS98 model prediction of the geocentric distance to the magnetopause (black curve) for the Cluster pressure; plasma ratios RI (red curve) and RE (blue curve, see details in the text); magnetic local time. LANL-1997 encountered with the magnetosheath at  $\sim 0530$ MLT.

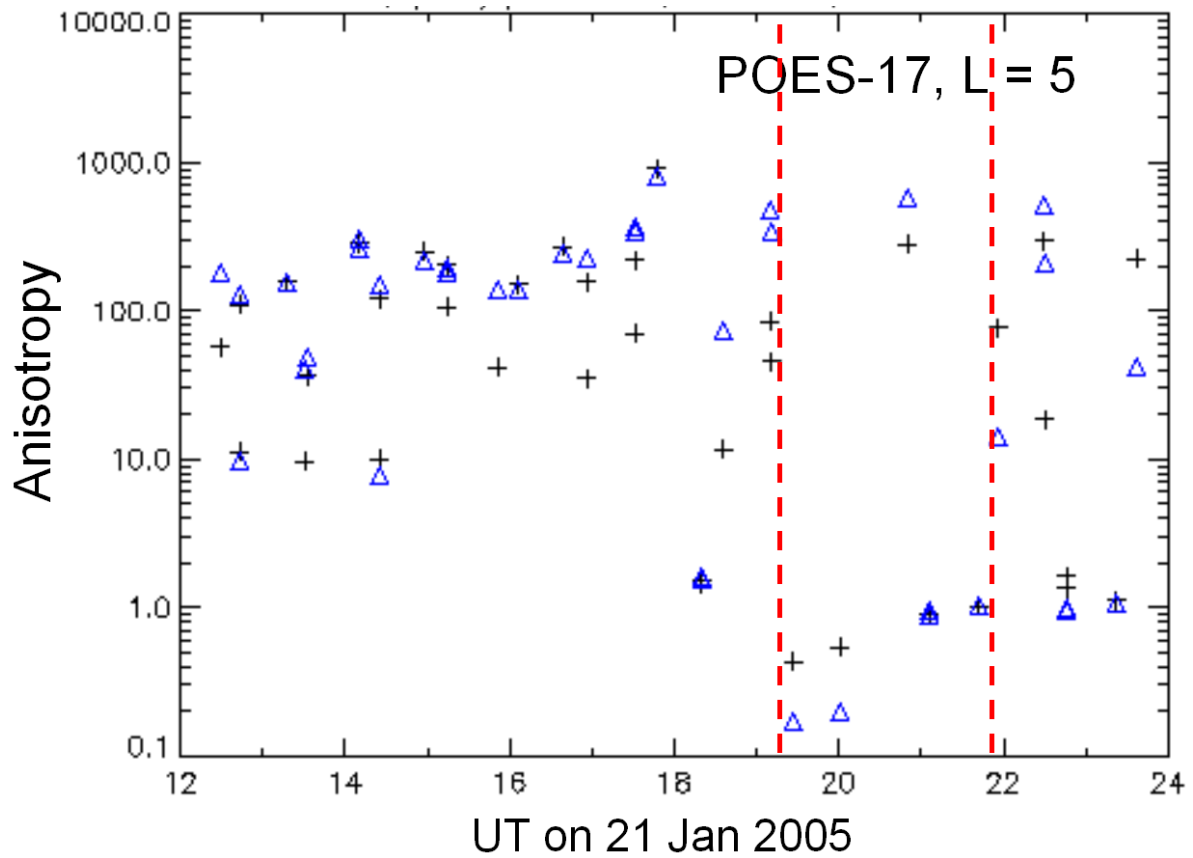


Figure 6. Temporal dynamics of pitch-angle anisotropy for the protons with energies  $>30$  keV (black crosses) and  $>100$  keV (blue triangles) observed by POES-17 near the noon-midnight meridian at  $L \sim 5$  on 21 January 2005. From  $\sim 19$  to  $\sim 22$  UT (restricted by red dashed lines), the anisotropy was less than or about 1 indicating that the majority of protons were not trapped at  $L \sim 5$ .

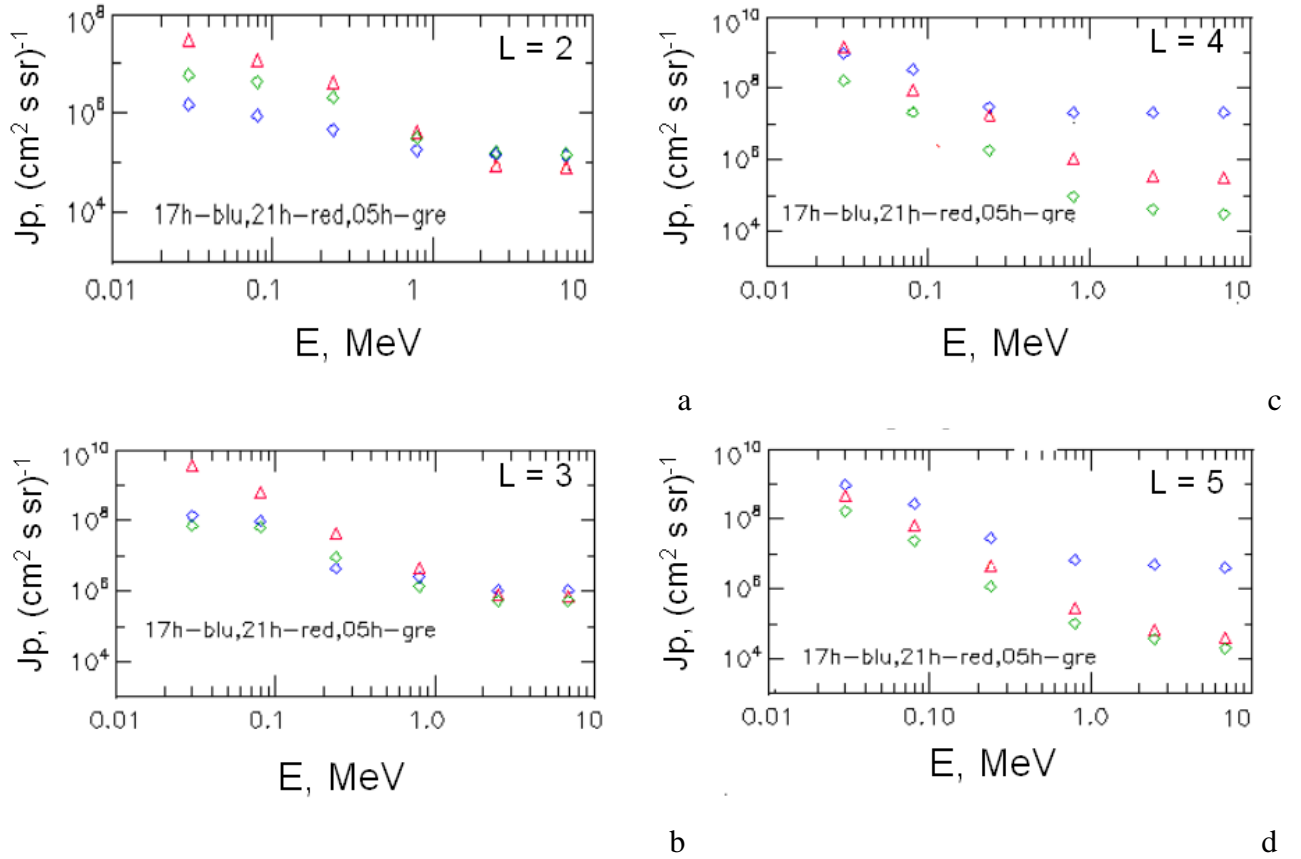


Figure 7. Dynamics of proton integral spectra observed by POES-17 satellite near the noon-midnight meridian on 21 – 22 January 2005: (a) at  $L = 2$ ; (b) at  $L = 3$ ; (c) at  $L = 4$ ; (d) at  $L = 5$ . Different symbols and colors correspond to different observation times: blue diamonds – 17 UT, red triangles – 21 UT on 21 January and green diamonds – 05 UT on 22 January. At 21 UT, the fluxes of low-energy protons ( $<1$  MeV) increased in the inner magnetosphere ( $L < 4$ ) by more than 10 times.

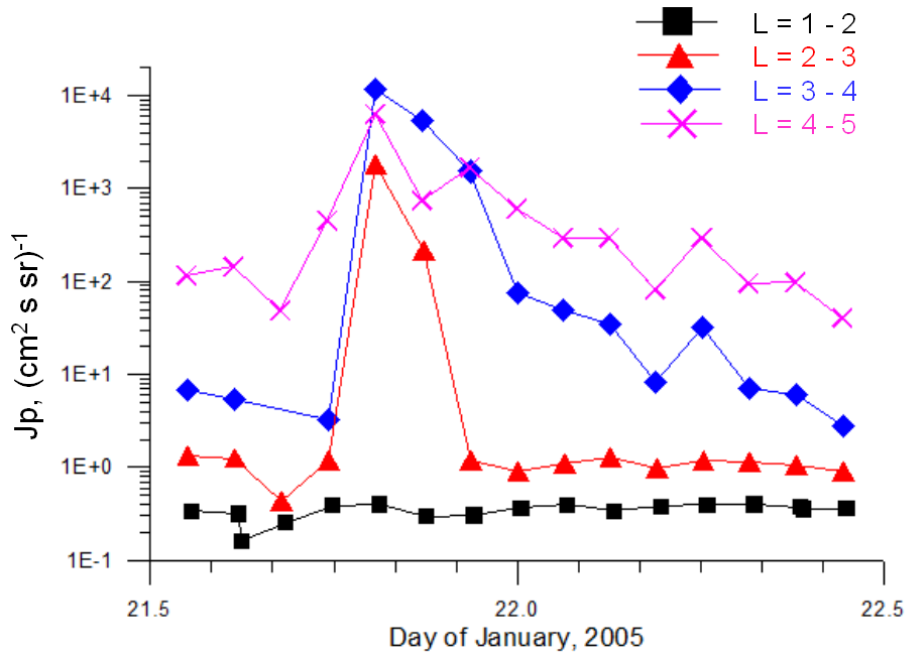


Figure 8. Temporal variations of 1 – 5 MeV protons observed by CORONAS-F satellite on 21 – 22 January, 2005. Black curve with squares corresponds to a region of  $L = 1 - 2$ , red curve with triangles –  $L = 2 - 3$ , blue curve with diamonds –  $L = 3 - 4$ , and pink curve with crosses –  $L = 4 - 5$ . After 18UT on 21 January, the proton fluxes increased substantially in the inner magnetosphere.



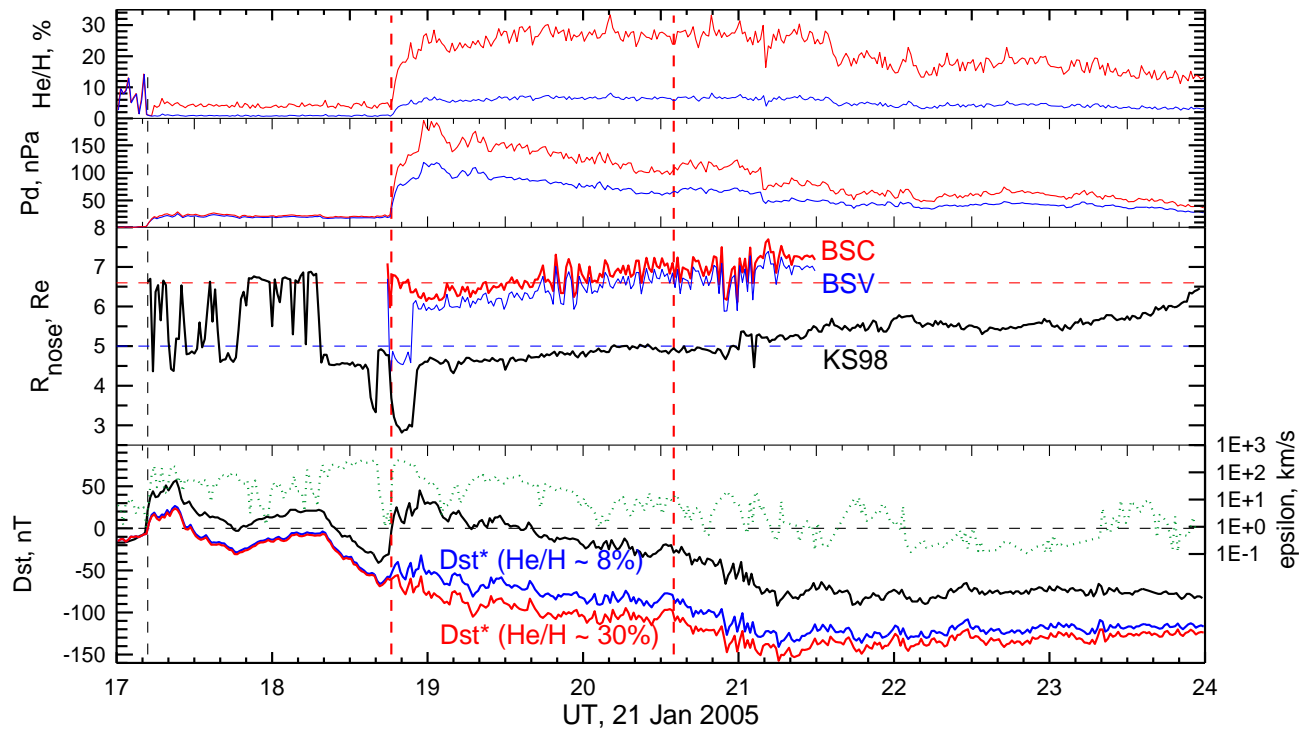


Figure 9. Observed and proposed variations of the solar wind plasma and geomagnetic parameters on 21 January 2005 (from top to bottom): helium contribution  $\text{He}/\text{H}$  measured by Cluster C4 (blue curve) and 4-time magnified one (red curve); solar wind dynamic pressure  $P_d$  calculated from Cluster C-4 data (blue curve) and with using the magnified  $\text{He}/\text{H}$  (red curve); nose distances to the bow shock and magnetopause predicted by the models BSC (red curve), BSV (blue curve) and KS98 (black curve) for the magnified  $\text{He}/\text{H}$ ;  $Dst$  variation observed (black curve) and normalized by the observed  $P_d$  (blue curve) and by the magnified  $P_d$  (red curve) as well as a driving parameter  $\varepsilon$  for the tail current (dotted green curve, right axis). The vertical red dashed lines restrict the interplanetary interval when the subsolar magnetopause was located upstream of the bow shock. The assumption of strong helium contribution of  $\sim 30\%$  allows resolving the discrepancies between the observations and model predictions.

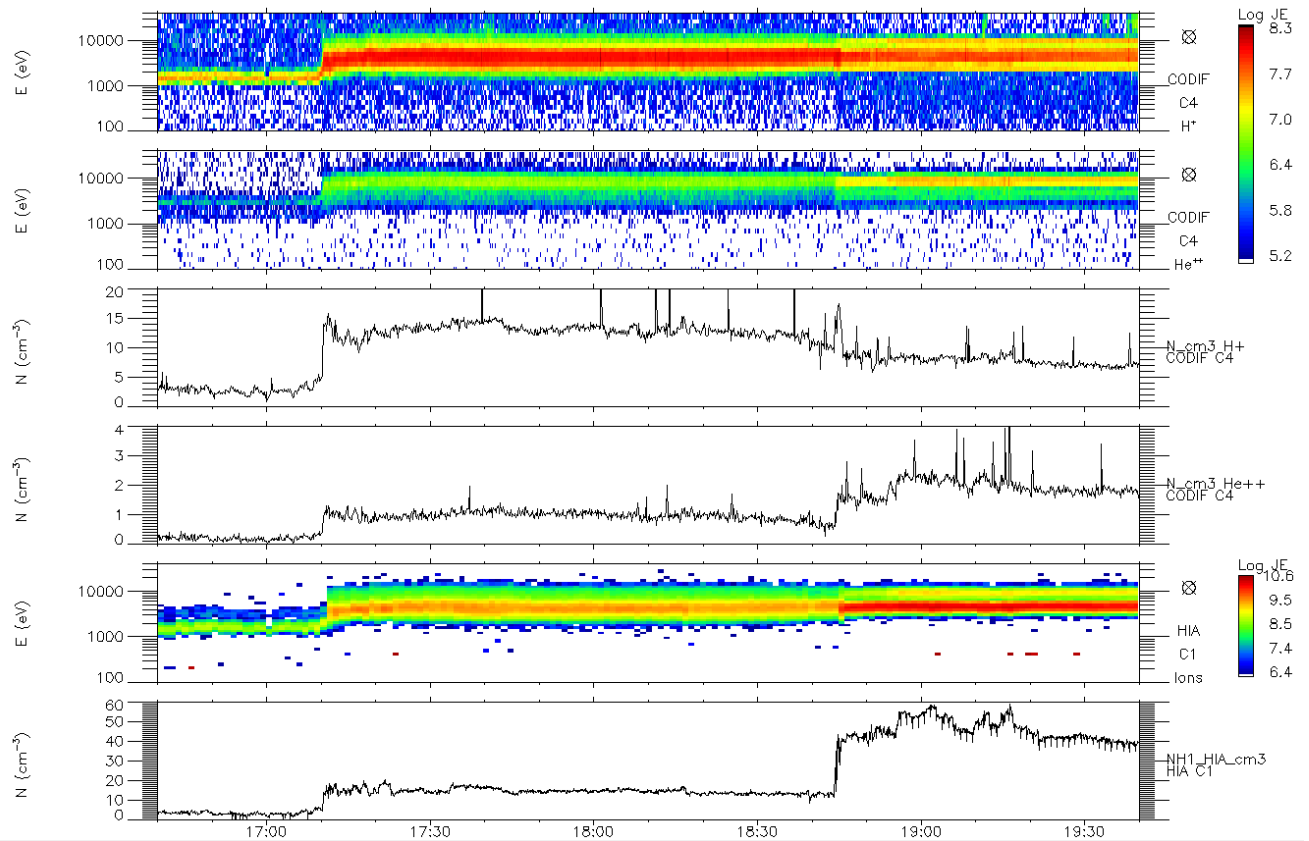


Figure 10. Variations of plasma parameters measured by Cluster on 21 January 2005 (from top to bottom): CODIF C4 energy-time spectrograms (in particle energy flux units) for H<sup>+</sup> and He<sup>++</sup>; the corresponding densities of H<sup>+</sup> and He<sup>++</sup>; Cluster C1 HIA (no mass discrimination) ion energy-time spectrogram and corresponding density. The data come from the more recent calibrations of the CIS team (acquired from private communication with anonymous Reviewer of this paper).